Mixed conductivity, thermochemical expansion and electrochemical activity of Fe-substituted $(La,Sr)(Cr,Mg)O_{3-\delta}$ for solid oxide fuel cell anodes

CrossMark

A.A. Yaremchenko [a,*], V.V. Kharton [a], V.A. Kolotygin [a], M.V. Patrakeev [b], E.V. Tsipis [a,c], J.C. Waerenborgh [c]

[a] Department of Materials and Ceramic Engineering, CICECO, University of Aveiro, 3810-193 Aveiro, Portugal
[b] Institute of Solid State Chemistry, UB RAS, 91 Pervomayskaya Str., 620219 Yekaterinburg, Russia
[c] IST/ITN, Instituto Superior Técnico, Universidade Técnica de Lisboa, CFMC-UL, EN 10, 2686-953 Sacavém, Portugal

HIGHLIGHTS

- $(La_{0.9}Sr_{0.1})_{0.98}Cr_{0.9-x}Fe_xMg_{0.1}O_{3-\delta}$ ($x = 0-0.3$) are stable under SOFC anode operation conditions.
- Iron cations substitute in 3+ oxidation state in both oxidized and reduced materials.
- Substitution with Fe increases oxygen deficiency and ionic transport under reducing conditions.
- The materials exhibit moderate TECs and small chemical expansion on reduction.
- Porous anodes ($x = 0.3$) show good electrochemical performance in contact with LSGM.

ARTICLE INFO

ABSTRACT

The effect of iron substitution in perovskite-type $(La_{0.9}Sr_{0.1})_{0.98}Cr_{0.9-x}Fe_xMg_{0.1}O_{3-\delta}$ ($x = 0-0.3$) is evaluated with emphasis on the properties relevant for solid oxide fuel cell anode application including the phase stability, oxygen nonstoichiometry, mixed ionic−electronic transport, thermochemical expansion and electrochemical activity. Thermogravimetric analysis, Mössbauer spectroscopy and electrical measurements in combination with X-ray diffraction confirm the stability of perovskite phase for $x = 0.3$ down to $p(O_2)$ as low as 10^{-19} atm at 1223 K. Mössbauer spectroscopy results indicate also that iron cations substitute in 3+ oxidation state in both oxidized and reduced material. The total conductivity is predominantly p-type electronic, with negligible contribution of ionic transport under oxidizing conditions. Substitution with iron decreases electronic transport, but also leads to higher oxygen deficiency and ionic conductivity under reducing conditions. The oxygen nonstoichiometry variations, determined by coulometric titration, and defect chemistry of $(La_{0.9}Sr_{0.1})_{0.98}Cr_{0.6}Fe_{0.3}Mg_{0.1}O_{3-\delta}$ can be described by non-ideal solution model and site-exclusion effects. The materials exhibit moderate thermal expansion coefficients $(10.1−11.5) \times 10^{-6}$ K^{-1} in air, nearly independent of iron content and $p(O_2)$, and favorably small chemical expansion on reduction. Porous $(La_{0.9}Sr_{0.1})_{0.98}Cr_{0.6}Fe_{0.3}Mg_{0.1}O_{3-\delta}$ anodes applied onto $LaGaO_3$-based solid electrolyte with thin $Ce_{0.8}Gd_{0.2}O_{2-\delta}$ interlayers show a better electrochemical performance compared to $(La_{0.75}Sr_{0.25})_{0.95}Cr_{0.5}Mn_{0.5}O_{3-\delta}$ under identical conditions.

1. Introduction

Nickel-based composite anodes show a good electrochemical performance in H₂-based fuels and have been used in solid oxide fuel cell (SOFC) prototypes for decades. Their often-cited drawbacks include however poor redox stability and large dimensional changes in inevitable redox cycles leading to microstructural and functional degradation [1]. These cermets suffer also from the fast coking and sulfur poisoning in hydrocarbon fuels resulting in blocking of porous anodes and subsequent loss of performance [2]. Significant efforts are focused therefore on the development of alternative electrode components satisfying numerous requirements to SOFC anode such as phase stability and high electrical conductivity under fuel atmosphere conditions, chemical and

* Corresponding author. Tel.: +351 234 370235; fax: +351 234 370204.
E-mail address: ayaremchenko@ua.pt (A.A. Yaremchenko).

thermomechanical compatibility with solid electrolytes, and superior electrochemical activity. A number of perovskite-like oxide ceramic materials with electronic or mixed ionic-electronic conductivity are considered as potential substituents for nickel in anodes. Representative examples include donor-doped $SrTiO_3$, $Sr_2MgMoO_{6-\delta}$, and solid solutions derived from $SrVO_{3-\delta}$ and $LaCrO_3$ [3–5].

$LaCrO_3$ and, in particular, its alkaline earth-substituted derivatives exhibit an attractive combination of properties making them not only the SOFC interconnect candidate materials [6], but also promising hosts for the development of ceramic anodes. They are stable in both oxidizing and reducing atmospheres and exhibit moderate thermal expansion compatible with that of common solid electrolytes [3–6]. Acceptor-type substitutions with calcium, strontium or magnesium result in improvement of electrical conductivity [6]. Furthermore, Sr- and Ca-substituted lanthanum chromites do not catalyze carbon deposition [7,8] and thus are potential anode materials for direct oxidation of methane-based fuels. Although the electrocatalytic activity of $(La,Sr)CrO_3$-based anodes is often poor [9,10], the performance can be improved by appropriate substitutions into chromium sublattice, provided that its excellent redox stability is retained. One example of efficient anode material is $(La_{1-x}Sr_x)_{1-y}Cr_{0.5}Mn_{0.5}O_{3-\delta}$ ($x = 0.2$–0.25, $y = 0$–0.1) perovskite which demonstrated fairly good electrochemical activity in both hydrogen and wet CH_4 [11–16], and also was suggested for use in symmetrical cells with anode and cathode made of the same material [13]. One drawback of this material is relatively low electronic conductivity in both oxidizing and reducing conditions in combination with p-type conduction behavior [16]. As a result, infiltration of metals (e.g. Cu, Ni) as electronic current collectors and/or electrocatalytically-active additives (e.g., $CeO_{2-\delta}$) are required to minimize anode ohmic and polarization resistance [14–16]. Positive results were also obtained for iron-substituted $(La,Sr)CrO_{3-\delta}$ [17–20]; in particular, $La_{0.75}Sr_{0.25}Cr_{0.5}Fe_{0.5}O_{3-\delta}$ electrodes showed lower polarization resistance in symmetrical cells with $LaGaO_3$-based solid electrolyte if compared to the Mn-containing analog [18]. The electrochemical cells with iron-containing electrodes exhibit however a higher series resistance, presumably due to stronger interaction between electrodes and solid electrolyte [18]. Note that introducing a ceria-based buffer layer between lanthanum gallate-based electrolyte and $La_{0.75}Sr_{0.25}Cr_{0.5}Mn_{0.5}O_{3-\delta}$ electrodes was reported to prevent diffusion of Cr and Mn cations into electrolyte surface layers [14].

The present work was aimed on the appraisal of iron-substituted $(La_{0.9}Sr_{0.1})_{0.95}Cr_{0.9}Mg_{0.1}O_{3-\delta}$ for possible use as a SOFC anode material. The main attention was focused on the properties relevant for practical application including phase relationships in different atmospheres, ionic and electronic transport properties in connection with the oxygen nonstoichiometry variations and defect chemistry mechanism, thermochemical expansion, and electrochemical behavior. A particular concern is given to stability issues under highly reducing conditions assessed employing a series of techniques including Mössbauer spectroscopy. Note that the low-$p(O_2)$ stability of $(La,Sr)CrO_{3-\delta}$ heavily substituted with iron is questionable [19–21]. For instance, it was reported that the XRD pattern of $La_{0.75}Sr_{0.25}Cr_{0.5}Fe_{0.5}O_{3-\delta}$ annealed in 5%H_2 at 1173 K for 120 h shows the trace amounts of metallic iron [19]. In another report [21], XRD analysis of $La_{0.75}Sr_{0.25}Cr_{0.5}Fe_{0.5}O_{3-\delta}$ quenched from 1173 K and $p(O_2) = 10^{-20}$ atm demonstrated the segregation of $(La,Sr)_2FeO_4$ secondary phase. Haag et al. [20] indicated that $LaSr_2Fe_2CrO_{9-\delta}$ starts to decompose at $p(O_2) < 10^{-20}$ atm at 1073 K. In the present work, iron concentration was limited therefore to 30 at.% in chromium sublattice. $La_{0.9}Sr_{0.1}Cr_{0.9}Mg_{0.1}O_{3-\delta}$ with a moderate content of acceptor-type dopants, Sr^{2+} and Mg^{2+}, in both sublattices was selected as a parent composition. Minor cation deficiency was also

introduced into the A-sublattice in order to decrease the chemical expansion on reduction [11]. The electrochemical activity of porous anode layers was evaluated in contact with two selected solid electrolytes – perovskite-type $(La_{0.9}Sr_{0.1})_{0.98}Ga_{0.8}Mg_{0.2}O_{3-\delta}$ (LSGM) and apatite-type $La_{10}Si_5AlO_{26.5}$ (LSA) ([22] and references therein). Thin $Ce_{0.8}Gd_{0.2}O_{2-\delta}$ (CGO) buffer interlayer was introduced between electrodes and electrolytes, similar to the previous reports [16,17,23].

2. Experimental

The powders of $(La_{0.9}Sr_{0.1})_{0.98}Cr_{0.9-x}Fe_xMg_{0.1}O_{3-\delta}$ ($x = 0$–0.3) were synthesized by the glycine-nitrate self-combustion technique using metal nitrates as oxidant and glycine as fuel and chelating agent. Appropriate proportions of metal nitrates (Sigma–Aldrich) and glycine (SAFC) were dissolved in distilled water. The solution was stirred at room temperature for several hours, and then heated on a hot plate until auto-ignition. The foam-like combustion products were ground and annealed in air at 1273 K for 2 h in order to burn out organic residues. Dense disk-shaped ceramic samples were pressed uniaxially at 40 MPa and sintered in air for 5 h; the sintering temperatures are listed in Table 1. Prepared ceramic samples were cut into rectangular bars and polished for the electrical and dilatometric measurements. The experimental density was calculated from the mass and geometric dimensions of the samples. Powdered samples for X-ray diffraction (XRD), Mössbauer spectroscopy and thermal (TGA/DSC) analysis were prepared by grinding sintered ceramics in a mortar with subsequent annealing (air, 1273 K, 2 h) and slow cooling in order to attain equilibrium with atmospheric oxygen pressure at low temperatures.

Room-temperature and high-temperature XRD patterns were recorded using Rigaku D/Max-B (CuK$_\alpha$, $2\Theta = 10$–$80°$, step $0.02°$, exposition 3 s) and Philips X'pert MPD (CuK$_\alpha$, $2\Theta = 10$–$80°$, step $0.02°$, exposition 15 s) diffractometers, respectively. Unit cell parameters were calculated from the XRD data using Fullprof software (profile matching method). Microstructural characterization was performed by scanning electron microscopy (SEM, Hitachi S-4100 instrument) coupled with energy dispersive spectroscopy (EDS, Rontec UHV detector). Differential scanning calorimetry (DSC) studies were done in air using Netzsch 204HP equipment (300–873 K, 5 K min^{-1}). The dilatometric measurements (vertical Linseis L75V/1250 instrument) and thermogravimetric analysis (TGA, Setaram SetSys 16/18 instrument) were carried out in flowing air, argon, 10%H_2–N_2 and CO–CO_2 mixtures at 298–1373 K with constant heating/cooling rate of 2–3 K min^{-1} or isothermally as function of time. In all cases, the oxygen partial pressure, $p(O_2)$, in a gas atmosphere was monitored using yttria-stabilized zirconia (YSZ) solid-electrolyte sensors; $p(O_2)$ in 10%H_2–N_2 flow corresponded to $\sim 10^{-19}$ atm at 1173 K.

The Mössbauer spectra were collected at room temperature and at 4.2 K; details may be found in Refs. [24,25]. The measurements were performed in transmission mode using a conventional constant-acceleration spectrometer and a 25 mCi ^{57}Co source in a Rh matrix. The velocity scale was calibrated using α-Fe foil. The absorbers were obtained by pressing the powdered samples into perspex holders. Isomer shifts (IS) are given relative to metallic α-Fe

Table 1
Properties of as-prepared $(La_{0.9}Sr_{0.1})_{0.98}Cr_{0.9-x}Fe_xMg_{0.1}O_{3-\delta}$ ceramics.

x	$T_{sintering}$, K	Density ρ_{exp}, g cm^{-2}	ρ_{exp}/ρ_{theor}, %	Unit cell parameters		
				a, Å	b, Å	c, Å
0	2023	5.72	88.4	5.4774(3)	7.7542(4)	5.5199(3)
0.1	2023	6.08	94.1	5.4855(3)	7.7646(4)	5.5250(3)
0.2	2023	6.38	99.1	5.4943(3)	7.7748(4)	5.5295(3)
0.3	1973	6.37	99.0	5.5010(2)	7.7847(3)	5.5328(2)

at room temperature. The low-temperature spectra were collected using a JANIS bath cryostat, model SVT-400, with the sample immersed in liquid He. The spectra were fitted to Lorentzian lines using a non-linear least-squares method. In the course of refinement procedure, the relative areas and line widths of both peaks in a quadrupole doublet and peaks 1–6, 2–5 and 3–4 in a magnetic sextet were constrained to remain equal. Distribution of magnetic splittings was fitted according to the histogram method [26].

The oxygen nonstoichiometry (δ) variations with oxygen partial pressure were studied at 973–1223 K by coulometric titration (CT) technique using double electrochemical cells [27]. The titration was performed in isothermal regime at oxygen pressures from 0.9 atm down to 10^{-16}–10^{-20} atm. After each isothermal cycle, reversibility of the redox processes and reproducibility of the results were checked by pumping oxygen into the cell and re-measuring 3–8 data points. The reproducibility of δ values after redox cycles was within 0.002 oxygen atoms per formula unit. The reference point for the CT data arrays was selected at 1223 K and $p(O_2) \sim 0.9$ atm assuming that $\delta \to 0$ under these conditions.

Electrical conductivity (σ) was measured by 4-probe DC technique as function of temperature at 300–1770 K in air and Ar atmospheres, and by AC impedance spectroscopy (Agilent 4284A precision LCR meter) as function of time in $10\%H_2$–N_2 flow. The measurements of conductivity and Seebeck coefficient (S) as function of $p(O_2)$ were performed simultaneously at 973–1223 K in the $p(O_2)$ range from 0.35 down to $\sim 10^{-19}$ atm in O_2–CO_2 and CO–CO_2 atmospheres using a specially designed YSZ chamber [28]. The Seebeck coefficient values were corrected for the contribution of platinum leads. The criteria for equilibration after a change in either oxygen pressure or temperature included the relaxation rates of the conductivity and Seebeck coefficients less than 0.05% min^{-1} and 0.001 mV ($K^{-1} \times min^{-1}$), respectively.

The steady-state oxygen permeation fluxes through dense ceramic membranes were studied as a function of temperature and $p(O_2)$ gradient at 1073–1248 K. In all cases, the oxygen partial pressure at the membrane feed side (p_2) was equal to 0.21 atm; the membrane thickness (d) varied from 0.50 to 1.00 mm. Prior to the measurements, the gas-tightness of disk-shaped ceramic membranes was verified by the absence of physical leakages under the total pressure gradient 2–3 atm at room temperature. In oxidizing conditions corresponding to permeate-side oxygen pressures (p_1) from 0.02 to 0.11 atm, the measurements were carried out using YSZ electrochemical cells equipped with one oxygen pump and one sensor [29]. The determination of oxygen permeation fluxes under air/(H_2–H_2O) gradients was based on the analysis of the oxygen activity in the gas mixture flowing over the membrane permeate side. The experimental setup comprised a dense membrane disk hermetically sealed onto the YSZ tube using glass sealant, and two YSZ oxygen sensors at the cell inlet and outlet [29]. The inlet 10% H_2–N_2 mixture flow rate was fixed using a Bronkhorst mass-flow controller, and additionally measured by a soap-film flow meter. The oxygen permeation flux density (j) was calculated from the $p(O_2)$ values at the inlet and outlet, and inlet gas flow rate.

The steady-state anodic polarization measurements were performed employing 3-electrode technique and using the electrochemical cells comprising solid electrolyte membrane, symmetrical porous working and counter electrodes made of $(La_{0.9}Sr_{0.1})_{0.98}Cr_{0.6}Fe_{0.3}Mg_{0.1}O_{3-\delta}$ and Pt, respectively, CGO interlayer between solid electrolyte and working electrode, and porous Pt reference electrode. Pt gauze was used as current collectors. The cell configuration and measuring procedures were identical to those described in Ref. [16]. For fabrication of working electrode, as-synthesized $(La_{0.9}Sr_{0.1})_{0.98}Cr_{0.6}Fe_{0.3}Mg_{0.1}O_{3-\delta}$ powder was annealed in air at 1473 K for 10 h to achieve the phase homogeneity. CGO interlayers (3–5 mg cm^{-2}) and $(La_{0.9}Sr_{0.1})_{0.98}Cr_{0.6}$

$Fe_{0.3}Mg_{0.1}O_{3-\delta}$ working electrodes (25 $\pm$ 2 mg cm^{-2}) were consecutively applied onto LSGM or LSA solid electrolytes and sintered in air for 2 h at 1473 K and 1423 K, respectively. The anodes were reduced in-situ in $10\%H_2$–N_2 atmosphere at 1073 K for 24 h before starting the measurements. The polarization studies were performed in galvanostatic mode using an Autolab PGSTAT302 instrument at 973–1073 K in flowing wet $10\%H_2$–N_2 gas mixture (H_2:H_2O $\sim$ 1.2). The ohmic (R) and polarization (R_η) resistances were determined from the impedance spectra collected in the frequency range from 10 mHz to 1 MHz. After a measurement cycle, working electrodes were surface-modified with $CeO_{2-\delta}$ by impregnation with saturated ethanol solution of cerium nitrate followed by nitrate thermal decomposition, and the measurements were repeated.

3. Results and discussion

3.1. Crystal structure and ceramic microstructure

Room-temperature XRD analysis confirmed that all sintered ceramics were single-phase with orthorhombically-distorted perovskite-type structure (space group Pnma); one example of XRD pattern is shown in Fig. 1A. The calculated unit cell parameters were found to reasonably increase with iron substitution (Table 1) due to larger ionic radius of Fe^{3+} cations (high-spin state) compared to Cr^{3+} and Cr^{4+} [30].

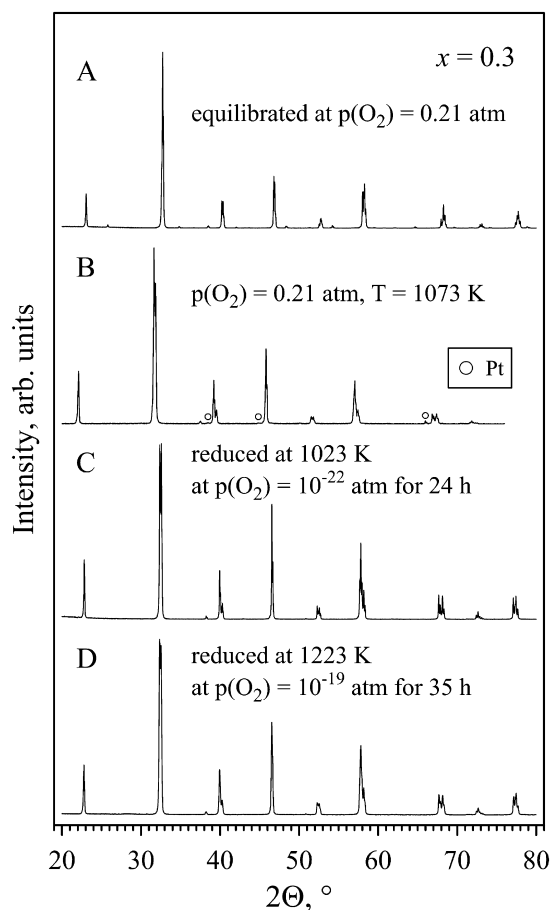DSC analysis of powdered ceramic samples indicated an appearance of reversible phase transition on heating in air. The

Fig. 1. Room-temperature (A, C, D) and high-temperature (B) XRD patterns of $(La_{0.9}Sr_{0.1})_{0.98}Cr_{0.6}Fe_{0.3}Mg_{0.1}O_{3-\delta}$ after treatment in different conditions.

Table 2
Structural transition temperatures and average TECs of $(La_{0.9}Sr_{0.1})_{0.98}Cr_{0.9-x}Fe_xMg_{0.1}O_{3-\delta}$ ceramics.

x	T of structural transition, K (±5) ($p(O_2) = 0.21$ atm)		Average thermal expansion coefficient		
	DSC	Dilatometry	$p(O_2)$, atm	T range, K	$(\overline{\alpha} \pm 0.1) \times 10^6$, K^{-1}
0	333	339	0.21	413–923 / 923–1373	10.1 / 10.9
0.1	404	406	0.21	313–398 / 443–923 / 923–1373	7.4 / 10.4 / 11.2
0.2	474	475	0.21	313–468 / 503–923 / 923–1373	7.7 / 10.5 / 11.5
0.3	545	545	0.21	313–533 / 573–923 / 923–1373	8.0 / 10.8 / 11.5
			5×10^{-5}	573–923 / 923–1373	10.4 / 11.4[b]
			3%CO–CO$_2$[a]	573–923 / 923–1373	10.3 / 10.8[b]

[a] $p(O_2) = 10^{-12}$ atm at 1223 K.
[b] On cooling.

results of high-temperature XRD studies (Fig. 1B) showed that, similar to parent LaCrO$_3$ [31], this transition is associated with the transformation from orthorhombically-distorted perovskite at lower temperatures to rhombohedral structure (space group $R\overline{3}c$). Note that the substitution with magnesium into chromium sublattice of LaCrO$_3$ is known to shift the phase transition from $\sim$535 K to higher temperatures, while substitution with strontium into lanthanum sublattice has an opposite effect [32,33]. In the present case, substitution of chromium with iron results in progressive increase of the structural transition temperature from 333 K for $(La_{0.9}Sr_{0.1})_{0.98}Cr_{0.9}Mg_{0.1}O_{3-\delta}$ up to 545 K for material with $x = 0.3$ (Table 2).

Sintering of iron-free chromite yielded ceramic samples with the relative density slightly under 90% (Table 1). Substitution with iron resulted in improved sinterability under similar conditions (Fig. 2); consequently, dense ceramics with homogeneous microstructure and negligible porosity were obtained for the materials containing 20 and 30 at.% of iron in B sublattice. The average grain size increased from $\sim$3.5 μm for $x = 0$ to $\sim$6 μm for $x = 0.3$ (Table 3).

3.2. Phase stability under reducing conditions

Room-temperature XRD analysis of $(La_{0.9}Sr_{0.1})_{0.98}Cr_{0.9-x}Fe_xMg_{0.1}O_{3-\delta}$ powdered samples after treatment in flowing 10%H$_2$–N$_2$ gas mixture at 1023–1223 K for 24–35 h showed no signs of phase decomposition, even for $x = 0.3$ (Fig. 1C and D). Reduced samples exhibited rhombohedrally-distorted perovskite structure similar to the high-temperature modification of oxidized samples, with no traces of phase impurities. The calculations showed $\sim$1% increase of the pseudocubic unit cell volume at room temperature after reduction.

Isothermal thermogravimetric studies at 1223 K confirmed the phase stability at reduced $p(O_2)$. In particular, switching from oxidizing to reducing atmosphere resulted in a rapid change of samples mass attributed to changing oxidation state of the transition metal cations and oxygen release from the lattice (Fig. 3A). After a fast relaxation (2–3 h), samples mass and, therefore, oxygen nonstoichiometry values remained constant on further isothermal treatment under these conditions suggesting the absence of any slow decomposition or lattice reconstruction processes. Thus, thermogravimetric analysis in combination with XRD results indicate that the title materials are thermodynamically stable under reduced oxygen partial pressures characteristic for SOFC anode operation conditions.

3.3. Mössbauer spectroscopy

The results of Mössbauer spectroscopy studies of powdered $(La_{0.9}Sr_{0.1})_{0.98}Cr_{0.6}Fe_{0.3}Mg_{0.1}O_{3-\delta}$ are summarized in Table 3 and Fig. 4. The spectra of air-equilibrated material recorded at 295 K and 4.2 K, below the magnetic transition temperature, may be fitted to a
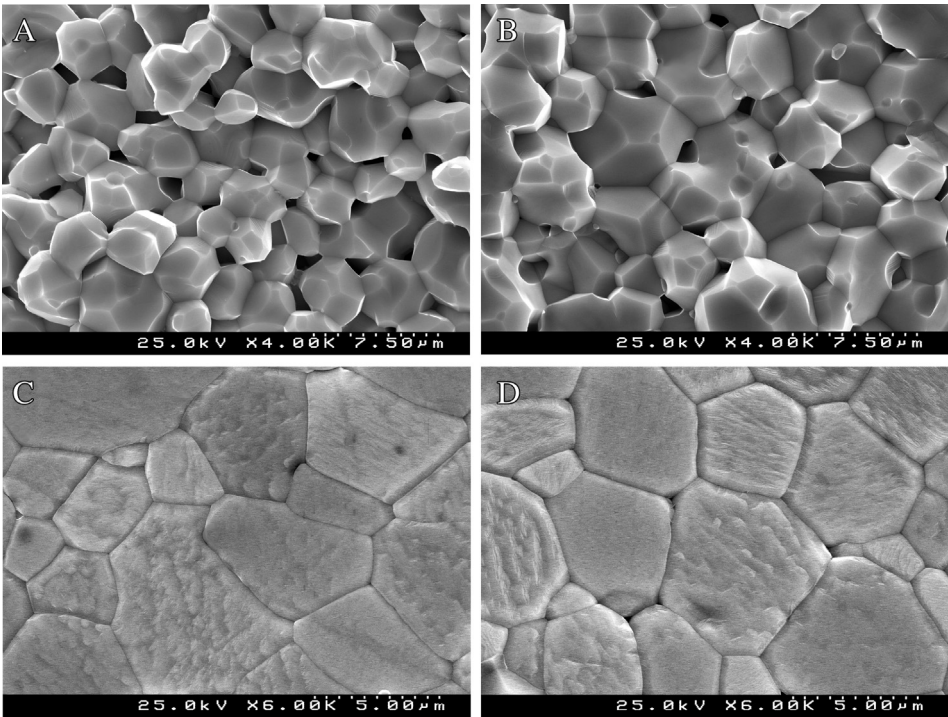
Fig. 2. SEM micrographs: fractured (A, B) and polished and thermally-etched (C, D) $(La_{0.9}Sr_{0.1})_{0.98}Cr_{0.9-x}Fe_xMg_{0.1}O_{3-\delta}$ ceramics with $x = 0$ (A), $x = 0.1$ (B), $x = 0.2$ (C) and $x = 0.3$ (D).
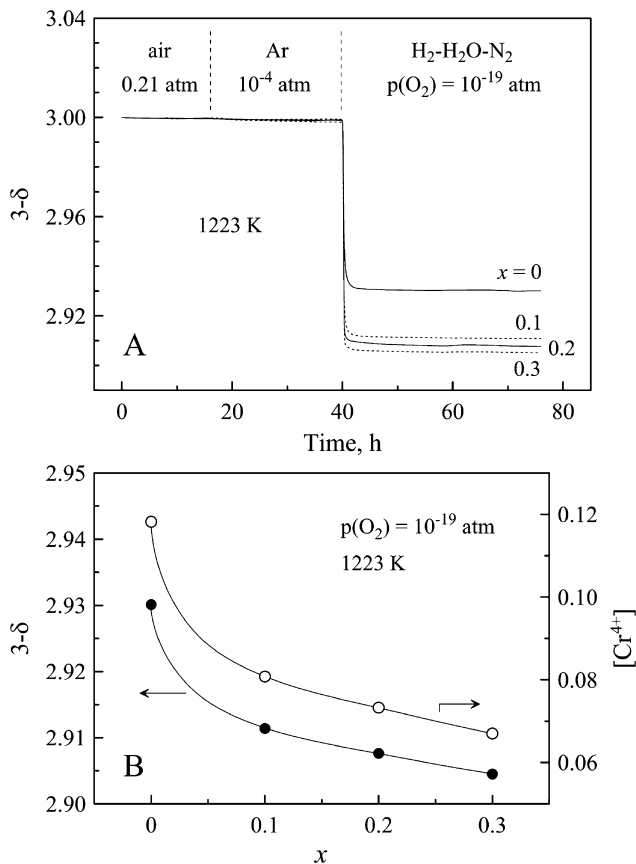
Table 3
Parameters[a] estimated from the Mössbauer spectra of $(La_{0.9}Sr_{0.1})_{0.98}Cr_{0.6}Fe_{0.3}Mg_{0.1}O_{3-\delta}$ at 295 and 4 K.

Processing conditions	T, K	IS, mm s^{-1}	QS, mm s^{-1}	2ε, mm s^{-1}	B_{hf}, T	I, %	CN
Equilibrated	295	0.36	0.38	–	–	100	6
with air	4	0.49[b]	–	−0.05	47.2[b]	100	6
Reduced in flowing	295	0.37	0.31	–	–	62	6
10% H$_2$−N$_2$ (1223		0.28	1.11	–	–	38	5
K, $p(O_2)$ =	4	0.49	–	−0.03	49.8	64	6
5×10^{-18} atm, 24 h)		0.41	–	−0.17	46.1	36	5

[a] IS, QS, $2\varepsilon = (e^2V_{ZZ}Q/4) \times (3\cos^2\theta - 1)$, B_{hf}, I and CN are the isomer shift, quadrupole splitting, quadrupole shift, magnetic hyperfine field, relative area and coordination number of trivalent iron, respectively. Estimated errors are ≤ 0.2 T for B_{hf}, <2% for I, and ≤ 0.02 mm s^{-1} for other parameters.
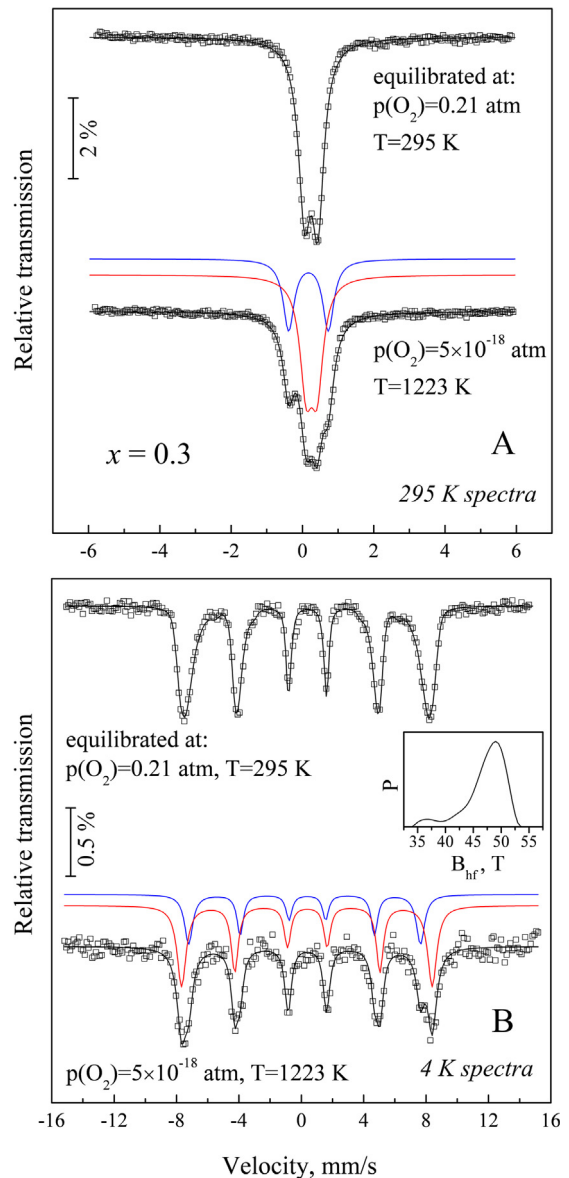[b] Average values of a magnetic sextet distribution.

quadrupole doublet and a distribution of magnetic sextets, respectively. The calculated isomer shifts (IS) and average magnetic hyperfine field (B_{hf}) values (Table 3) are typical for octahedrally-coordinated Fe^{3+} in oxides [24,25,34,35]. The doublet at 295 K is asymmetric (Fig. 4A) which may be explained by a narrow distribution of quadrupole splittings caused by chemical disorder rather than by the presence of an overlapping Fe^{4+} contribution with lower IS. The difference in the second and third cation-coordination spheres of Fe^{3+} surrounded by 4 types of B-site species (Cr^{3+}, Cr^{4+}, Fe^{3+} and Mg^{2+}) and 3 types of A-site neighbors (La, Sr, cation vacancies) give rise to slightly different, unresolved quadrupole

interactions. The signal asymmetry results from small IS differences of the different Fe environments. The same reason is responsible for the distribution of magnetic splittings observed at 4.2 K (Fig. 4B). IS values estimated both at 295 and 4 K are typical of hexa-coordinated Fe^{3+} cations. The contributions with low relative area and lower B_{hf} visible in the calculated probability distribution (inset in Fig. 4B) can be ascribed to Mg^{2+} in the nearest neighborhood of octahedrally-coordinated Fe^{3+}, which hinders magnetic exchange interactions. No Fe^{4+} is therefore detected by the Mössbauer spectra analysis in oxidized sample, thus suggesting that the acceptor charge compensation in $(La,Sr)(Cr,Fe,Mg)O_{3-\delta}$ occurs primarily via Cr^{4+} formation.

The spectra of $(La_{0.9}Sr_{0.1})_{0.98}Cr_{0.6}Fe_{0.3}Mg_{0.1}O_{3-\delta}$ reduced at $p(O_2) = 5 \times 10^{-18}$ atm and 1223 K may be adequately described by two quadrupole doublets at room temperature and two magnetic

Fig. 3. Variations of oxygen nonstoichiometry in $(La_{0.9}Sr_{0.1})_{0.98}Cr_{0.9-x}Fe_xMg_{0.1}O_{3-\delta}$ on reduction at 1223 K (A), and dependence of oxygen nonstoichiometry and Cr^{4+} concentration on iron content under reducing conditions at 1223 K (B). All data are calculated from the thermogravimetric results (see text).

Fig. 4. Mössbauer spectra of $(La_{0.9}Sr_{0.1})_{0.98}Cr_{0.6}Fe_{0.3}Mg_{0.1}O_{3-\delta}$ equilibrated with air at low temperature or reduced at 1223 K in 10%H$_2$−N$_2$ flow, recorded at room temperature (A) and at 4 K (B). The lines plotted over the experimental points are the quadrupole doublet or the sum of two doublets (A), and the magnetic hyperfine field distribution or the sum of two magnetic sextets (B) shown shifted for clarity. Inset shows the probability distribution of the magnetic hyperfine fields.

sextets at 4.2 K (Fig. 4). The two subspectra are attributed to 6- and 5-fold coordinated Fe^{3+} cations since the difference in their IS values, $0.08-0.09$ mm s^{-1}, is similar to that usually observed for Fe^{3+} between these coordinations and too small compared to that observed between octahedral and tetrahedral Fe^{3+} states [24,25,34,35]. In addition to lower IS, the signal of penta-coordinated Fe^{3+} has a higher quadrupole splitting (QS), as expected for a site with more distorted oxygen polyhedra compared to $Fe^{3+}O_6$ octahedra. The relationship between 6- and 5-fold co-ordinated Fe^{3+} concentrations is close to the [Cr]/([Fe]+[Mg]) ratio (Table 3); this may indicate that oxygen vacancies are preferably located between iron and magnesium cations, whilst $Cr^{3+/4+}$ species form relatively stable metal-oxygen octahedra. Neither metallic iron nor Fe^{2+} can be detected in the reduced material.

For $(La_{0.9}Sr_{0.1})_{0.98}Cr_{0.6}Fe_{0.3}Mg_{0.1}O_{3-\delta}$ reduced at 1023 K in flowing 10%H_2-N_2 mixture with $p(O_2) = 10^{-22}$ atm, the spectra were found identical to those of the sample reduced at 1223 K, within the limits of experimental uncertainties. In all cases, no evidence of phase decomposition due to reduction was revealed by the Mössbauer spectroscopy.

3.4. Oxygen nonstoichiometry and defect chemistry

The results of thermogravimetric measurements indicated very negligible variations of oxygen nonstoichiometry in air. For all $(La_{0.9}Sr_{0.1})_{0.98}Cr_{0.9-x}Fe_xMg_{0.1}O_{3-\delta}$, the changes of oxygen content on heating to 1273 K corresponded to ≤ 0.0006 atoms per formula unit.

Fig. 5A shows the $p(O_2)-T-\delta$ diagram of the composition with $x = 0.3$ at $1023-1223$ K obtained by the coulometric titration technique. Acceptor-doped lanthanum chromites demonstrate typically a plateau-like behavior of $\delta-p(O_2)$ dependencies in high $p(O_2)$ region and, applying $|\partial\delta/\partial p(O_2)|_{min}$ criterion as an indication of stoichiometric composition, are considered therefore as oxygen-stoichiometric under these conditions [36,37]. From the same considerations, it was assumed that $\delta \to 0$ in $(La_{0.9}Sr_{0.1})_{0.98}Cr_{0.6}Fe_{0.3}Mg_{0.1}O_{3-\delta}$ at 1223 K and $p(O_2) \sim 0.9$ atm; this state was used as a reference for the experimental CT data set. Deviations from the oxygen stoichiometry at this oxygen partial pressure for different temperatures were <0.001 atom per formula unit during the entire experiment.

$(La_{0.9}Sr_{0.1})_{0.98}Cr_{0.6}Fe_{0.3}Mg_{0.1}O_{3-\delta}$ exhibits very minor variations of oxygen content at $1023-1223$ K under oxidizing conditions. Increase of δ with decreasing oxygen pressure from atmospheric to $\sim 10^{-5}$ atm corresponds to approximately 0.002 for all temperatures and is comparable with reproducibility error. The behavior of $(La_{0.9}Sr_{0.1})_{0.98}Cr_{0.6}Fe_{0.3}Mg_{0.1}O_{3-\delta}$ under reducing conditions is qualitatively very similar to that of other acceptor-doped lanthanum chromites reported in literature (Fig. 5B). Reducing $p(O_2)$ below $10^{-5}-10^{-10}$ atm results in progressive increase of oxygen deficiency in the perovskite lattice (Fig. 5A). The onset of reduction is shifted to higher $p(O_2)$ if compared to $La_{0.8}Sr_{0.2}CrO_{3-\delta}$ and $La_{0.8}Ca_{0.2}CrO_{3-\delta}$ with similar acceptor-type dopant concentration, but corresponds to more reducing conditions in comparison with $La_{0.75}Sr_{0.25}Cr_{0.5}Fe_{0.5}O_{3-\delta}$ (Fig. 5B).

Defect chemistry of $(La_{0.9}Sr_{0.1})_{0.98}Cr_{0.9-x}Fe_xMg_{0.1}O_{3-\delta}$ (or $La_{1-y-y'}Sr_yCr_{1-x-z}Fe_xMg_zO_{3-\delta}$) can be described using the formalism proposed by Mizusaki et al. for $La_{1-x}A_xCrO_{3-\delta}$ (A = Sr, Ca) assuming non-ideal solution behavior [36,37]. Considering $LaCrO_3$ as a host matrix, the major point defects include Sr cations (Sr'_{La}) and cation vacancies (V'''_{La}) in the lanthanum sublattice, Cr^{4+} (or $Cr^{\bullet}_{Cr}$) and magnesium (Mg'_{Cr}) cations on Cr^{3+} sites, and oxygen vacancies ($V^{\bullet\bullet}_O$). Taking into account the results of Mössbauer spectroscopy, isovalent Fe^{3+} cations can be excluded from the defect equilibrium in a first approximation. The oxygen exchange reaction between the oxide lattice and gas phase can be expressed by

$$2Cr^{\times}_{Cr} + V^{\bullet\bullet}_O + 0.5O_2 \Leftrightarrow 2Cr^{\bullet}_{Cr} + O^{\times}_O \quad (1)$$
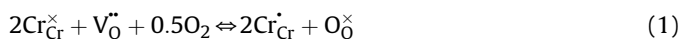
with the corresponding equilibrium constant

$$K = \frac{[Cr^{\bullet}_{Cr}]^2 [O^{\times}_O]}{[Cr^{\times}_{Cr}]^2 [V^{\bullet\bullet}_O]} \frac{1}{p(O_2)^{1/2}} \frac{\gamma_2^2 \gamma_3}{\gamma_1^2 \gamma_4} \quad (2)$$

where γ_1, γ_2, γ_3 and γ_4 are the activity coefficients of $Cr^{\times}_{Cr}$, $Cr^{\bullet}_{Cr}$, $O^{\times}_O$ and $V^{\bullet\bullet}_O$, respectively. The charge neutrality condition is given by:

$$[Sr'_{La}] + 3[V'''_{La}] + [Mg'_{Cr}] = [Cr^{\bullet}_{Cr}] + 2[V^{\bullet\bullet}_O] \quad (3)$$

Taking into account the definitions

$$[Sr'_{La}] = y; \quad [V'''_{La}] = y'; \quad [Mg'_{Cr}] = z; \quad [V^{\bullet\bullet}_O] = \delta \quad (4)$$

the concentration of Cr^{4+} cations can be expressed as

$$[Cr^{\bullet}_{Cr}] = y + 3y' + z - 2\delta \quad (5)$$
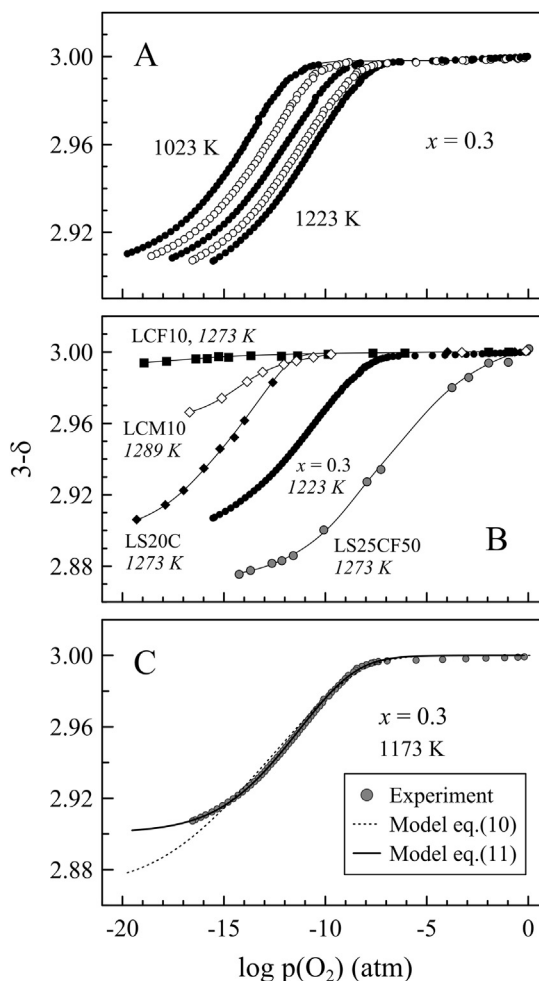
Fig. 5. Oxygen nonstoichiometry of $(La_{0.9}Sr_{0.1})_{0.98}Cr_{0.6}Fe_{0.3}Mg_{0.1}O_{3-\delta}$ determined by the coulometric titration technique: (A) $\delta-p(O_2)$ dependencies at $1023-1223$ K (the curves are given with 50 K interval); (B) comparison with other $LaCrO_3$-based perovskite-like oxides; (C) example of fitting the experimental data at 1173 K. The literature data on $La_{0.8}Sr_{0.2}CrO_{3-\delta}$ (LS20C [40]), $LaCr_{0.9}Mg_{0.1}O_{3-\delta}$ (LCM10 [38]), $LaCr_{0.9}Fe_{0.1}O_{3-\delta}$ (LCF10 [41]) and $La_{0.75}Sr_{0.25}Cr_{0.5}Fe_{0.5}O_{3-\delta}$ (LS25CF50 [21]) are shown for comparison.

Combining Eqs. (2) and (5) with the lattice site conservation conditions:

$$\left[O_O^\times\right] + \left[V_O^{\bullet\bullet}\right] = 3 \tag{6}$$

$$\left[Cr_{Cr}^\times\right] + \left[Cr_{Cr}^\bullet\right] = 1 - x - z \tag{7}$$

one can obtain the expression:

$$\begin{aligned}
\Delta G^0 = \Delta H^0 - T\Delta S^0 &= -RT\ln K \\
&= -RT\ln\left[\left(\frac{y + 3y' + z - 2\delta}{1 - x - 2z - y - 3y' + 2\delta}\right)^2 \left(\frac{3 - \delta}{\delta}\right) p(O_2)^{-1/2}\right] \\
&\quad - RT\ln\frac{\gamma_2^2\gamma_3}{\gamma_1^2\gamma_4}
\end{aligned} \tag{8}$$

where ΔG^0, ΔH^0 and ΔS^0 are the standard free energy change, enthalpy change and entropy change, respectively, of reaction (1). The second term in Eq. (8) was defined as the deviation from the standard free energy change of the ideal solution (ΔG_{dev}^0) which can be expressed as a linear function of oxygen nonstoichiometry [36,37]:

$$\Delta G_{dev}^0 = RT\ln\frac{\gamma_2^2\gamma_3}{\gamma_1^2\gamma_4} = a\delta \tag{9}$$

where a is a temperature-dependent constant representing the effect of defect interactions. From Eqs. (8) and (9), the relationship between oxygen partial pressure and the oxygen nonstoichiometry for the composition with $x = 0.3$ is given by:

$$p(O_2) = \left[\frac{1}{K}\left(\frac{0.258 - 2\delta}{0.342 + 2\delta}\right)^2 \left(\frac{3 - \delta}{\delta}\right)\exp\left(\frac{a\delta}{RT}\right)\right]^2 \tag{10}$$

This type of relationship implies that oxygen nonstoichiometry should asymptotically approach the value of $\delta = 0.129$ (Eq. (3)) on reduction, thus reflecting the transition from electronic to oxygen-vacancy charge compensation mechanism and full depletion of Cr^{4+} cations. The experimental data indicate however that oxygen content in reduced $(La_{0.9}Sr_{0.1})_{0.98}Cr_{0.6}Fe_{0.3}Mg_{0.1}O_{3-\delta}$ tends to lower δ values, and Eq. (10) cannot adequately describe the $\delta-p(O_2)$ relationship (Fig. 5C). Careful inspection of literature data shows that a similar situation is observed for $LaCr_{1-x}Mg_xO_{3-\delta}$ perovskites, where oxygen deficiency also tends to lower values than predicted $\delta = 0.5x$ [38]. One may assume therefore that a fraction of Cr^{4+} cations is excluded from the defect equilibrium, e.g. due to formation of stable defect pairs such as $Cr^{4+}-O^{2-}-Mg^{2+}$. Consequently, the experimental data in the range of $\delta \sim 0.002-0.095$ were successfully fitted (Fig. 5C) using a slightly modified model:

$$p(O_2) = \left[\frac{1}{K}\left(\frac{0.258 - b - 2\delta}{0.342 + 2\delta}\right)^2 \left(\frac{3 - \delta}{\delta}\right)\exp\left(\frac{a\delta}{RT}\right)\right]^2 \tag{11}$$

where the temperature-dependent constant b corresponds to the fraction of tetravalent chromium cations not participating in oxygen exchange reaction. Parameters of model Eq. (11) obtained by fitting the experimental data are listed in Table 4. Estimated values of equilibrium constant K are lower compared to the corresponding values reported for $La_{1-x}A_xCrO_{3-\delta}$ (A = Ca, Sr) [36,37,39] thus reflecting easier reducibility of iron-substituted material and shift of $\delta-p(O_2)$ curves to higher oxygen pressures. The constant b was found to vary in the range 0.06–0.07 at 1023–1173 K slightly

Table 4
Parameters of fitting the oxygen nonstoichiometry data using model (11).

T, K	K	b (± 0.0005)	a, J mol^{-2}	r^2
1173	$(1.39 \pm 0.02) \times 10^6$	0.0592	$-(11.9 \pm 0.5) \times 10^4$	0.9995
1123	$(3.81 \pm 0.09) \times 10^6$	0.0642	$-(8.8 \pm 0.6) \times 10^4$	0.9991
1073	$(1.10 \pm 0.03) \times 10^7$	0.0677	$-(7.2 \pm 0.8) \times 10^4$	0.9985
1023	$(3.99 \pm 0.09) \times 10^7$	0.0705	$-(5.5 \pm 0.5) \times 10^4$	0.9992

$\Delta H^0 = -222 \pm 3$ kJ mol^{-1}, $\Delta S^0 = 72 \pm 3$ J (mol^{-1} K^{-1}).
r^2 is the coefficient of determination.

decreasing with temperature. Note that the latter values are close to the fraction of Mg^{2+} cations neighboring Cr ions, if the cation distribution in B-sublattice is random, thus supporting the hypothesis about partial exclusion of Cr^{4+} from defect equilibrium. This also agrees with the Mössbauer spectroscopy results which suggest that oxygen vacancies preferentially occupy the sites between iron and magnesium cations. On the other hand, model (11) can not explain minor variations of oxygen nonstoichiometry under oxidizing conditions, with $p(O_2) > 10^{-6}$ atm (Fig. 5C). It is likely that iron cations are involved in defect equilibrium, for instance, via high-temperature charge disproportionation reaction:

$$2Fe_{Cr}^\times \Leftrightarrow Fe_{Cr}^\bullet + Fe_{Cr}' \tag{12}$$

and/or shift of redox equilibrium between transition metal cations:

$$Cr_{Cr}' + Fe_{Cr}^\times \Leftrightarrow Cr_{Cr}^\times + Fe_{Cr}' \tag{13}$$

resulting in more complex defect chemistry mechanism.

Under reducing conditions, the substitution with iron in $(La_{0.9}Sr_{0.1})_{0.98}Cr_{0.9-x}Fe_xMg_{0.1}O_{3-\delta}$ leads to a progressive increase of oxygen deficiency compared to Fe-free material under similar conditions (Fig. 3B). Assuming that in all substituted materials iron cations remain preferentially in the 3+ oxidation state under these conditions, increasing oxygen nonstoichiometry can be related to a continuous decrease of Cr^{4+} concentration with x. This, again, reflects the increasing reducibility of $LaCrO_3$-based perovskites and the weakening of the average $B^{4+/3+}-O^{2-}$ ionic bond strength with iron incorporation into B sublattice. One necessary note relates to the fast kinetics of equilibration on reduction (Fig. 3B). This behavior is different if compared to the $LaCrO_3$ derivatives with higher Sr concentration in the A sublattice, e.g. $(La_{0.75}Sr_{0.25})_{0.95}Cr_{1-x}Fe_xO_{3-\delta}$ [17] characterized with prolonged equilibration process, and may indicate a faster oxygen exchange kinetics and/or absence of slow phase-transition processes.

3.5. Thermochemical expansion

Fig. 6A shows the dilatometric curves of $(La_{0.9}Sr_{0.1})_{0.98}Cr_{0.9-x}Fe_xMg_{0.1}O_{3-\delta}$ ceramics in air. As for parent $LaCrO_3$ [31], iron-substituted ceramics exhibit an anomaly on the dL/L_0-T curves clearly associated with the orthorhombic-to-rhombohedral transition. The results indicate that these structural changes are accompanied with a minor reversible contraction of the lattice on heating, 0.02–0.03% in linear dimensions. The transition temperatures determined from the dilatometric data were found to be in excellent agreement with the DSC data (Table 2). Above the phase transition, all ceramics show nearly linear behavior with the thermal expansion coefficients (TECs) slightly increasing with temperature and with iron content. The latter trend is connected with the variations of the lattice parameters (Table 1) and reflects a general correlation between unit cell volume and thermal lattice expansion for the materials with the same crystal structure. Average TEC values are comparable with those of common solid electrolytes such as YSZ, LSGM, CGO and LSA [3,4,22], thus
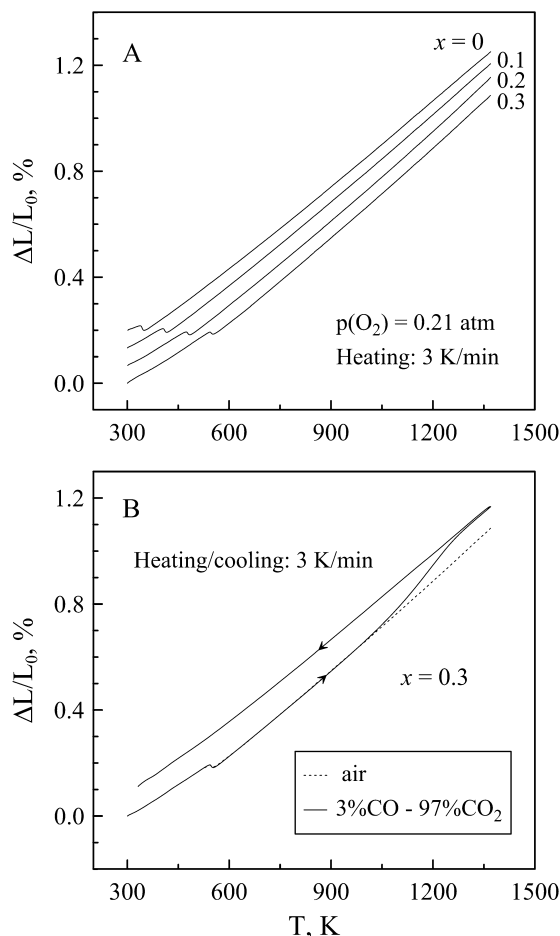
Fig. 6. Dilatometric curves of (A) $(La_{0.9}Sr_{0.1})_{0.98}Cr_{0.9-x}Fe_xMg_{0.1}O_{3-\delta}$ ceramics in air and (B) $(La_{0.9}Sr_{0.1})_{0.98}Cr_{0.6}Fe_{0.3}Mg_{0.1}O_{3-\delta}$ ceramics in different atmospheres.

providing thermomechanical compatibility between porous electrodes and dense electrolyte ceramics at elevated temperatures.

Heating in a reducing atmosphere above 973 K results in a noticeable expansion (Fig. 6B) caused by a chemical contribution. This contribution, or so-called chemical expansion, is associated with the oxygen release from the crystal lattice on reduction accompanied with the formation of oxygen vacancies and changes of oxidation state and, therefore, size of transition metal cations. The latter is considered to be the main cause of chemical expansion [42,43]. Reduced $(La_{0.9}Sr_{0.1})_{0.98}Cr_{0.9-x}Fe_xMg_{0.1}O_{3-\delta}$ demonstrate even slightly lower average TEC values in the high-temperature range (Table 2). One additional note is that the phase transition-related dimensional change is not observed on dilatometric curves of the samples equilibrated with reducing atmospheres (Fig. 6B). This confirms the XRD data indicating that the structural transition in reduced materials is shifted to temperatures below room temperature.

Fig. 7A shows the dependencies of isothermal chemical expansion (ε_C) of $(La_{0.9}Sr_{0.1})_{0.98}Cr_{0.6}Fe_{0.3}Mg_{0.1}O_{3-\delta}$ as function of oxygen partial pressure at 1223 and 1073 K. The value of ε_C is defined as:

$$\varepsilon_C = \frac{L - L_0^T}{L_0^T} \tag{14}$$

were L_0^T is the sample length at given temperature and reference $p(O_2)$ (atmospheric air in the present case). Under isothermal conditions, ceramic samples expectedly undergo chemical-induced

dimensional changes with reducing oxygen partial pressure, with shape of the curves resembling that of $\delta-p(O_2)$ dependencies (Fig. 5A). Similarly to other $LaCrO_3$-based perovskites, chemical strain of $(La_{0.9}Sr_{0.1})_{0.98}Cr_{0.6}Fe_{0.3}Mg_{0.1}O_{3-\delta}$ exhibit linear dependence if plotted against oxygen nonstoichiometry changes (Fig. 7B). This correlation can be expressed by a simple equation [39]:

$$\varepsilon_C = C \cdot \Delta\delta \tag{15}$$

where parameter C represents a measure of the lattice expansion per oxygen vacancy. Table 5 compares the values of this parameter reported in literature or calculated from the available data on $LaCrO_3$ derivatives. Some scattering originates mainly from the different methods used to obtain corresponding δ values (i.e. direct experimental measurements or calculations from available equilibrium constants). Nevertheless, analysis of the data indicates that acceptor-type doping into lanthanum sublattice increases the coefficient of chemical expansion, whilst the substitution with magnesium into chromium sites has an opposite effect. The latter was explained by the fact that substituting relatively large magnesium cations into chromium sublattice expands oxygen octahedra thus making the crystal structure less sensitive to increase of ionic size during the $Cr^{4+} \rightarrow Cr^{3+}$ reduction [42]. $(La_{0.9}Sr_{0.1})_{0.98}Cr_{0.6}Fe_{0.3}Mg_{0.1}O_{3-\delta}$ perovskite studied in this work represents an intermediate case, with the values of C favorably lower compared to most of reported lanthanum chromites at similar temperatures (Table 5). The coefficient of chemical expansion was found to increase slightly with decreasing temperature, in agreement with observed trend in
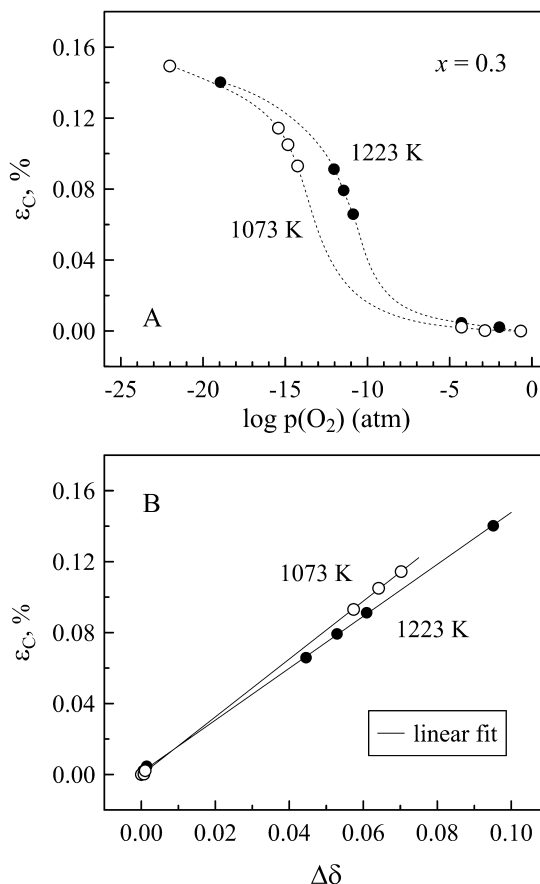
Fig. 7. Dependencies of chemical expansion of $(La_{0.9}Sr_{0.1})_{0.98}Cr_{0.6}Fe_{0.3}Mg_{0.1}O_{3-\delta}$ ceramics on oxygen partial pressure (A) and oxygen nonstoichiometry variations (B) at 1073 and 1223 K.

Table 5
Comparison of chemical expansion coefficient of LaCrO$_3$-based perovskites.

Composition	T, K	C = ε$_C$/Δδ	Ref.
(La$_{0.9}$Sr$_{0.1}$)$_{0.98}$Cr$_{0.6}$Fe$_{0.3}$Mg$_{0.1}$O$_{3-\delta}$	1223	0.0146	This work
	1073	0.0163	This work
La$_{0.9}$Sr$_{0.1}$CrO$_{3-\delta}$	1273	0.021	[39]
La$_{0.8}$Sr$_{0.2}$CrO$_{3-\delta}$	1273	0.028	[39]
	1273	0.016	[44]
	1273	0.023	[43]
	1273	0.027	[42]
	1073	0.024	[42]
La$_{0.7}$Sr$_{0.3}$CrO$_{3-\delta}$	1273	0.023	[44]
	1273	0.029	[42]
La$_{0.8}$Sr$_{0.2}$Cr$_{0.97}$V$_{0.03}$O$_{3-\delta}$	1273	0.027	[39]
	1273	0.027	[42]
	1073	0.029	[42]
La$_{0.9}$Ca$_{0.1}$CrO$_{3-\delta}$	1273	0.021	[43]
La$_{0.8}$Ca$_{0.2}$CrO$_{3-\delta}$	1273	0.026	[43]
	1273	0.021	[42]
La$_{0.7}$Ca$_{0.3}$CrO$_{3-\delta}$	1273	0.026	[42]
	1273	0.035	[44]
La$_{0.95}$Ca$_{0.05}$Cr$_{0.84}$Al$_{0.16}$O$_{3-\delta}$	1273	0.031	[43]
LaCr$_{0.95}$Mg$_{0.05}$O$_{3-\delta}$	1273	0.017	[42]
LaCr$_{0.85}$Mg$_{0.15}$O$_{3-\delta}$	1273	0.010	[42]
LaCr$_{0.79}$Mg$_{0.05}$Al$_{0.16}$O$_{3-\delta}$	1273	0.025	[43]

average TECs in different atmospheres. Note also that, under identical conditions, chemical expansion of (La$_{0.9}$Sr$_{0.1}$)$_{0.98}$Cr$_{0.6}$Fe$_{0.3}$Mg$_{0.1}$O$_{3-\delta}$ is twice lower compared to (La$_{0.75}$Sr$_{0.25}$)$_{0.95}$Mn$_{0.5}$Cr$_{0.5}$O$_{3-\delta}$ [16].

3.6. Electrical properties

Fig. 8A shows the temperature dependence of electrical conductivity of (La$_{0.9}$Sr$_{0.1}$)$_{0.98}$Cr$_{0.9-x}$Fe$_x$Mg$_{0.1}$O$_{3-\delta}$ ceramics in air. The total conductivity under these conditions is predominantly electronic. For instance, the analysis of oxygen permeation data (discussed below) indicate that oxygen-ionic contribution to the total conductivity of (La$_{0.9}$Sr$_{0.1}$)$_{0.98}$Cr$_{0.6}$Fe$_{0.3}$Mg$_{0.1}$O$_{3-\delta}$ corresponds to $\sim$0.0004% at 1248 K and decreases with decreasing temperature. The electronic transport in LaCrO$_3$-based perovskite is assumed to occur via electron–hole hopping between chromium cations, with Cr^{4+} (or Cr$^{\bullet}_{Cr}$) representing a p-type charge carrier localized on chromium ion [45,46]. At atmospheric oxygen pressure, all studied materials exhibit semiconducting behavior in the studied temperature range. Seebeck coefficient (S) measured at 973–1223 K was found to have a positive sign, thus confirming that electronic transport is p-type, and is almost independent of temperature. The obtained values of S in this temperature range corresponded to 172 ± 2 μV K^{-1} for x = 0 and 156 ± 2 μV K^{-1} for x = 0.3, slightly increasing on heating. As Seebeck coefficient is a function of charge carrier concentration according to the Heikes formula (e.g. Ref. [45]), its very weak dependence on temperature indicates nearly constant electron–hole concentration, in agreement with oxygen nonstoichiometry data.

The conductivity data of iron-free oxide, (La$_{0.9}$Sr$_{0.1}$)$_{0.98}$Cr$_{0.9}$Mg$_{0.1}$O$_{3-\delta}$, exhibit an ideally linear behavior if plotted in lnσT − 1/T coordinates (Table 6). This confirms that electronic transport in this material in air occurs via small-polaron hopping mechanism with temperature-independent charge-carrier concentration [46]. As iron cations in substituted materials exist solely in 3+ oxidation state (at least at lower temperatures), substitution with iron results in gradual decrease of electronic conductivity due to decreasing concentration of B-sites available for electron–hole hopping, and in increase of activation energy. On the other hand, the Arrhenius curves exhibit a break at $\sim$900–1070 K with increase of E$_A$ in high-temperature range (Table 6); the conductivities of all materials tend
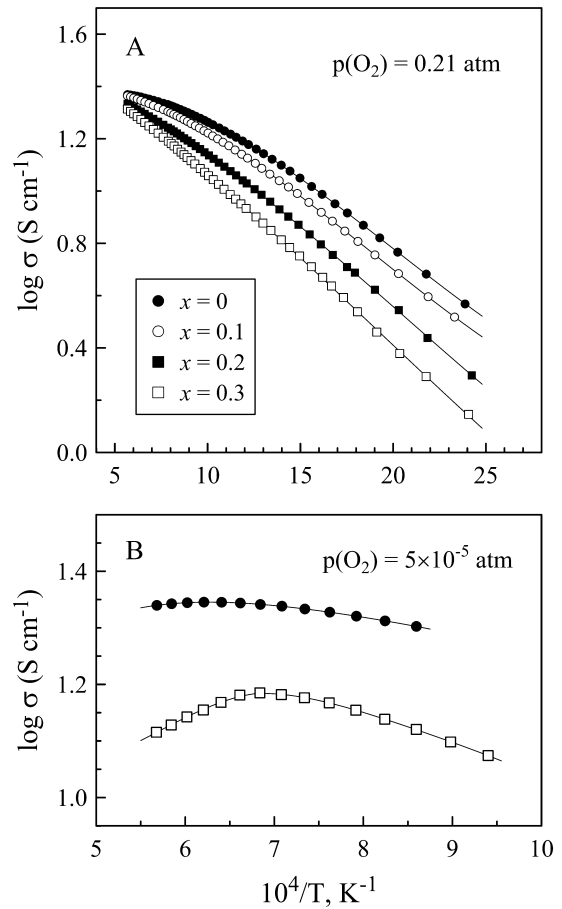
Fig. 8. Temperature dependencies of electrical conductivity of (La$_{0.9}$Sr$_{0.1}$)$_{0.98}$Cr$_{0.9-x}$Fe$_x$Mg$_{0.1}$O$_{3-\delta}$ ceramics (A) in air and (B) in inert gas atmosphere.

to similar values at temperatures above 1900 K. This implies that iron cations may in fact contribute to electronic transport process as well as to the defect equilibrium at high temperatures through e.g. reactions Eqs.12 and 13. Note that since iron cations concentration is below or close to percolation limit ($\sim$31% for cubic structure [45]), the electronic transport should involve charge carrier hopping between Fe and Cr ions.

The total conductivity (Fig. 9) and Seebeck coefficient of (La$_{0.9}$Sr$_{0.1}$)$_{0.98}$Cr$_{0.9-x}$Fe$_x$Mg$_{0.1}$O$_{3-\delta}$ were found nearly p(O$_2$)-independent at temperatures below 1273 K and oxygen pressures from 10^{-5} to 0.6 atm. This is, again, in agreement with the oxygen nonstoichiometry data indicating rather negligible variations of defect concentrations in this p(O$_2$)−T domain. Measurements of electrical conductivity in inert gas atmosphere with

Table 6
Activation energy for electrical conductivity of (La$_{0.9}$Sr$_{0.1}$)$_{0.98}$Cr$_{0.9-x}$Fe$_x$Mg$_{0.1}$O$_{3-\delta}$ ceramics in air.

Composition	Temperature range, K	E$_A$, kJ mol^{-1}	r^2
0	420−1760	15.06 ± 0.02	0.99991
0.1	420−900 / 900−1760	15.49 ± 0.07 / 16.91 ± 0.07	0.9996 / 0.9996
0.2	460−1070 / 1070−1760	16.90 ± 0.07 / 19.61 ± 0.12	0.9997 / 0.9994
0.3	460−1070 / 1070−1760	18.29 ± 0.08 / 22.32 ± 0.12	0.9995 / 0.9995

Note: the activation energy was calculated using Arrhenius model $\sigma = (A_0/T)\exp(-E_A/(RT))$.
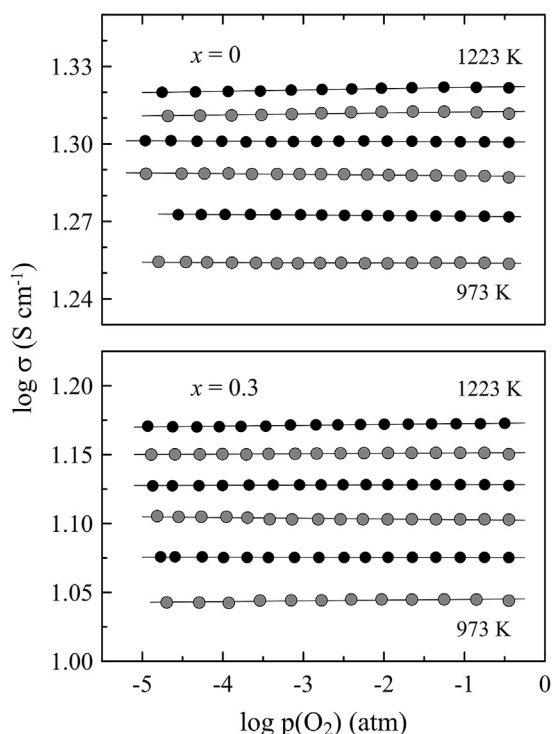
Fig. 9. Oxygen partial pressure dependencies of electrical conductivity of $(La_{0.9}Sr_{0.1})_{0.98}Cr_{0.9-x}Fe_xMg_{0.1}O_{3-\delta}$ ceramics at 973–1223 K under oxidizing conductions. The data are given with 50 K interval.

$p(O_2) \approx 5 \times 10^{-5}$ atm revealed a transition to pseudometallic behavior for $(La_{0.9}Sr_{0.1})_{0.98}Cr_{0.6}Fe_{0.3}Mg_{0.1}O_{3-\delta}$ on heating above ~ 1400 K (Fig. 8B). This apparent transition should be ascribed to the onset of reduction and, correspondingly, decrease of $[Cr^{4+}]$ and electronic conductivity above this temperature. Similar tendency is characteristic for iron-free material above ~ 1600 K at this $p(O_2)$.

At lower temperatures, 1073–1223 K, an onset of conductivity drop and transition to metallic-like behavior is observed on reducing oxygen partial pressure below 10^{-13}–10^{-8} atm (Figs. 10 and 11). In agreement with δ–$p(O_2)$ data (Fig. 5), substitution with iron shifts this onset to higher oxygen pressures. Decrease in the conductivity is accompanied with increasing Seebeck coefficient; this reflects the relationship between charge carrier concentration, $[Cr^{4+}]$, and oxygen deficiency, according to Eq. (5). For reduced materials, the conductivity becomes proportional to $p(O_2)^{1/4}$. This type of dependence can be expected if combining the definition

$$\sigma = e\mu_p p \tag{16}$$

(where μ_p and p are the mobility and concentration of p-type charge carriers, correspondingly) with the expression for equilibrium constant (Eq. (2)) under conditions when $[Cr^{4+}] << [Cr^{3+}]$ and variations of δ are small, i.e. for highly reduced materials. Another remark is that Seebeck coefficient of $(La_{0.9}Sr_{0.1})_{0.98}Cr_{0.6}Fe_{0.3}Mg_{0.1}O_{3-\delta}$ exhibits maximum at $p(O_2) \sim 10^{-18}$–10^{-17} atm at 1223 K and decreases on further reduction. As an appearance of n-type contribution is hardly expected under these conditions, this behavior of thermopower can be attributed to increasing role of ionic transport. The oxygen-ionic contribution to Seebeck coefficient is expected to have negative sign under reducing atmospheres [47].

As substitution with iron shifts the onset of reduction to higher oxygen partial pressures, this results in higher degree of reduction and, therefore, in lower concentration of charge carriers (Fig. 3B)
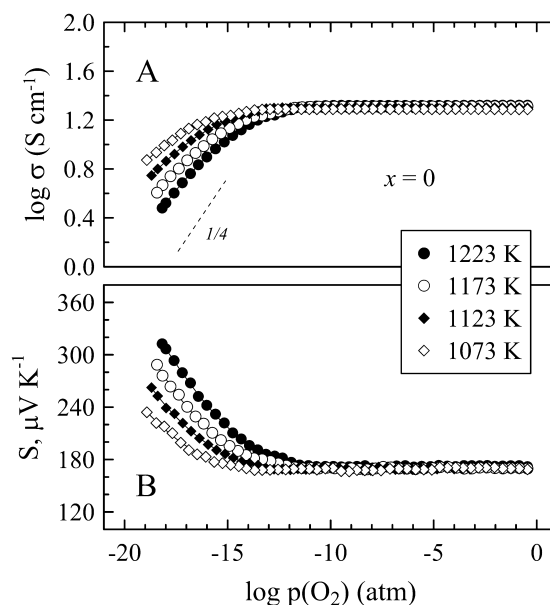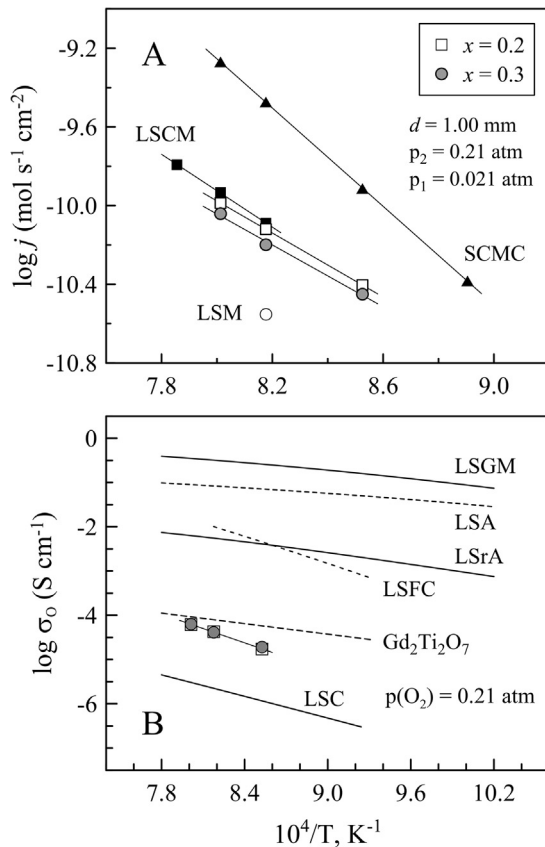

Fig. 10. Oxygen partial pressure dependencies of electrical conductivity (A) and Seebeck coefficient (B) of $(La_{0.9}Sr_{0.1})_{0.98}Cr_{0.9}Mg_{0.1}O_{3-\delta}$ ceramics at 1073–1223 K.

and lower conductivity (Figs. 10 and 11) at similar $p(O_2)$ under reducing conditions characteristic for SOFC anode operation. Thus, in wet hydrogen atmosphere (i.e. with $H_2:H_2O = 2:1$ ratio), the electrical conductivity of $(La_{0.9}Sr_{0.1})_{0.98}Cr_{0.6}Fe_{0.3}Mg_{0.1}O_{3-\delta}$ corresponds to approximately 0.75 and 0.50 S cm^{-1} at 1223 and 1123 K,
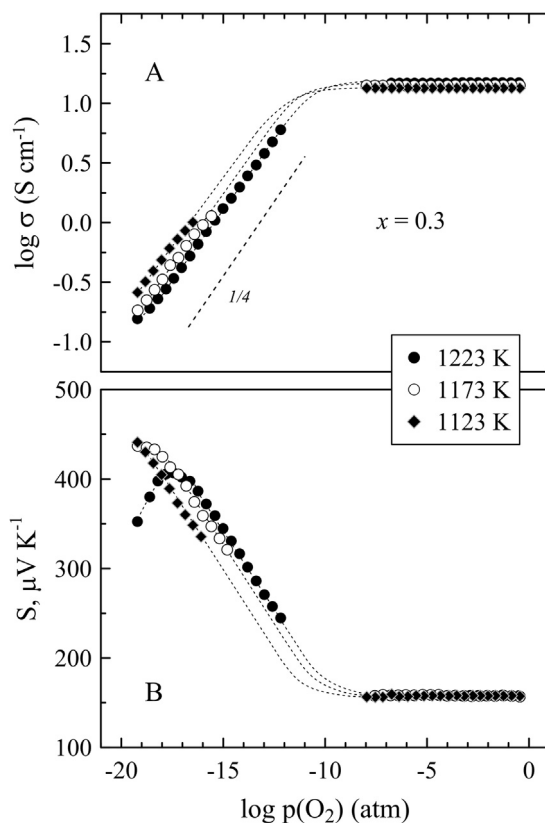
Fig. 11. Oxygen partial pressure dependencies of electrical conductivity (A) and Seebeck coefficient (B) of $(La_{0.9}Sr_{0.1})_{0.98}Cr_{0.6}Fe_{0.3}Mg_{0.1}O_{3-\delta}$ ceramics at 1123–1223 K. The dotted lines are a guide for the eye.
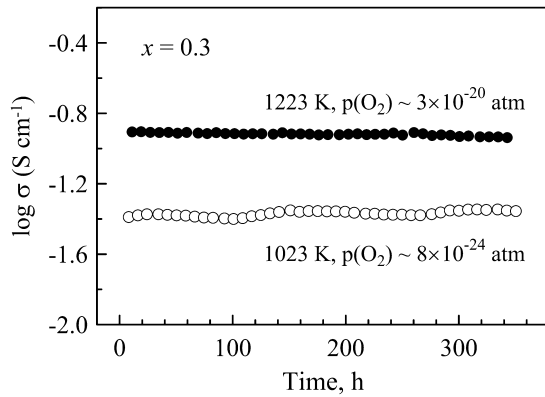
Fig. 12. Time dependencies of electrical conductivity of $(La_{0.9}Sr_{0.1})_{0.98}Cr_{0.6}Fe_{0.3}Mg_{0.1}O_{3-\delta}$ ceramics in dry $10\%H_2-N_2$ atmosphere at 1023 and 1223 K.

respectively. Note that the minimum electronic conductivity required to minimize the ohmic losses of SOFC anode corresponds to >1 S cm^{-1} for porous structures and one order of magnitude higher value for bulk materials [48]. Relatively low electronic conductivity of iron-substituted $(La,Sr)(Cr,Mg)O_{3-\delta}$ under reducing conditions may constitute therefore a performance-limiting factor for porous anode layers.

Fig. 12 demonstrates the time dependence of electrical conductivity of $(La_{0.9}Sr_{0.1})_{0.98}Cr_{0.6}Fe_{0.3}Mg_{0.1}O_{3-\delta}$ under highly reducing conditions (dry diluted hydrogen) at 1223 and 1023 K. No degradation of electrical properties with time was observed. Minor variations of conductivity are associated with the drifts of $p(O_2)$ in the gas flow. These results confirm once again the sufficient stability of Fe-substituted chromites in reducing atmospheres characteristic for SOFC anode operation.
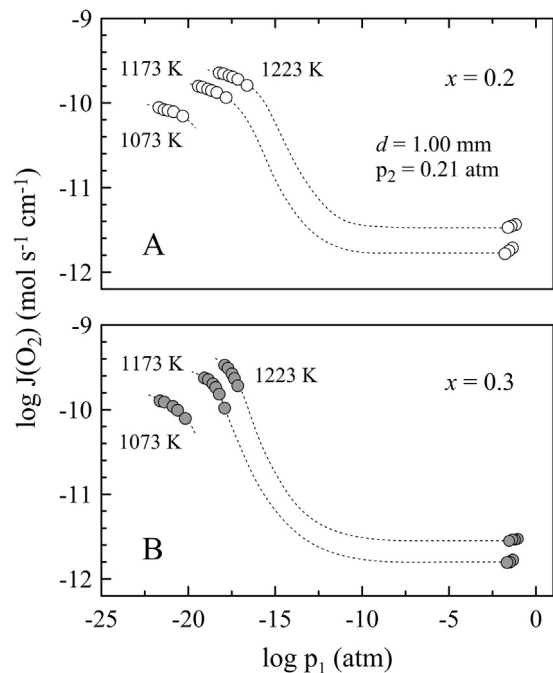
3.7. Oxygen-ionic transport

Fig. 13A shows temperature dependencies of oxygen permeation flux density (j) through dense $(La_{0.9}Sr_{0.1})_{0.98}Cr_{0.9-x}Fe_x$ $Mg_{0.1}O_{3-\delta}$ ($x = 0.2$ and 0.3) membranes under oxidizing conditions at fixed oxygen partial pressure gradient across the membrane. As for other chromites and manganites with very low or negligible concentration of oxygen vacancies in the perovskite lattice, iron-substituted $(La,Sr)(Cr,Mg)O_{3-\delta}$ display low values of oxygen permeability, slightly above the lower measurable limit of the applied technique. As $\delta \rightarrow 0$ under these conditions, the permeation process is expected to occur predominantly via grain boundary diffusion of oxygen ions, as was demonstrated e.g. for $La_{0.7}Ca_{0.3}CrO_3$ [49]. This may explain, in particular, minor decrease of oxygen permeation flux through ceramic membranes with increasing iron content. As discussed above, iron substitution promotes grain growth and therefore decreases grain boundary area.

The permeation flux density through the membrane bulk can be expressed by Wagner's equation [50]:

$$j = \frac{RT}{16F^2d} \int_{p1}^{p2} \sigma_{amb} \partial \ln p(O_2) \qquad (17)$$

where the ambipolar conductivity, σ_{amb}, is a function of partial oxygen-ionic and electronic contributions:

Fig. 13. Temperature dependencies of (A) oxygen permeation fluxes through dense $(La_{0.9}Sr_{0.1})_{0.98}Cr_{0.9-x}Fe_xMg_{0.1}O_{3-\delta}$ ceramic membranes under fixed $p(O_2)$ gradient, and (B) oxygen-ionic conductivity in these materials in air estimated from the oxygen permeation data. The literature data on $La_{0.7}Sr_{0.3}MnO_3$ (LSM), $(La_{0.75}Sr_{0.25})_{0.95}Cr_{0.5}Mn_{0.5}O_{3-\delta}$ (LSCM), $Sr_{0.7}Ce_{0.3}Mn_{0.7}Cr_{0.3}O_{3-\delta}$ (SCMC), LSGM, LSA, $La_{0.9}Sr_{0.1}AlO_{3-\delta}$ (LSrA), $La_{0.8}Sr_{0.2}Fe_{0.8}Co_{0.2}O_{3-\delta}$ (LSCF), $Gd_2Ti_2O_7$ and $La(Sr)CrO_3$ (LSC) are taken from Refs. [16,22,51,52].

Fig. 14. Dependencies of specific oxygen permeability of dense $(La_{0.9}Sr_{0.1})_{0.98}Cr_{0.9-x}Fe_xMg_{0.1}O_{3-\delta}$ ceramic membranes on permeate-side oxygen partial pressure at 1073–1223 K. The dotted lines are a guide for the eye.
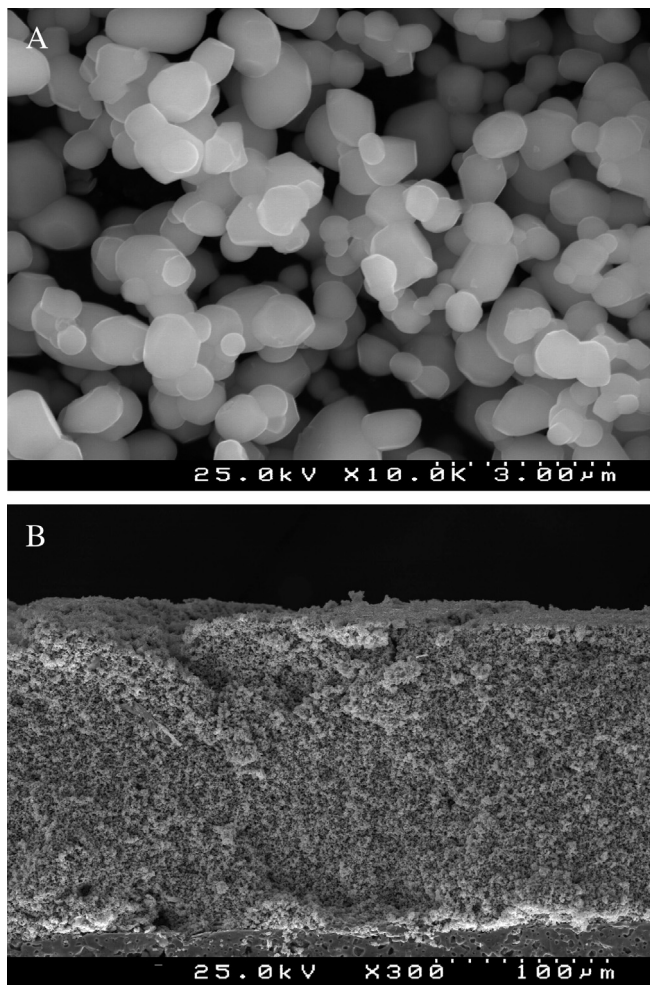
Fig. 15. SEM micrographs of (A) $(La_{0.9}Sr_{0.1})_{0.98}Cr_{0.6}Fe_{0.3}Mg_{0.1}O_{3-\delta}$ powder calcined at 1473 K for 10 h, and (B) cross-section of porous $(La_{0.9}Sr_{0.1})_{0.98}Cr_{0.6}Fe_{0.3}Mg_{0.1}O_{3-\delta}$ electrode layer on solid electrolyte with CGO interlayer.

$$\sigma_{amb} = \sigma_O\sigma_e/(\sigma_O + \sigma_e) \quad (18)$$

Fig. 13B compares oxygen-ionic conductivity of $(La_{0.9}Sr_{0.1})_{0.98}Cr_{0.9-x}Fe_xMg_{0.1}O_{3-\delta}$, roughly estimated using Eqs.17 and 18 and neglecting the surface exchange kinetics, with that of other solid electrolytes and mixed conductors at atmospheric oxygen pressure. Overall bulk ionic conductivity of the studied materials in air corresponds to $\sim(2-6) \times 10^{-5}$ S cm^{-1} at 1173–1248 K, being comparable to that of $(La_{0.75}Sr_{0.25})_{0.95}Cr_{0.5}Mn_{0.5}O_{3-\delta}$ [16].

Reducing oxygen partial pressure increases oxygen deficiency in the $(La_{0.9}Sr_{0.1})_{0.98}Cr_{0.9-x}Fe_xMg_{0.1}O_{3-\delta}$ crystal lattice and should improve, therefore, the ionic transport. Fig. 14 demonstrates the variations of specific oxygen permeability, $J(O_2)$, of iron-substituted ceramic membranes with $p(O_2)$ at the membrane permeate-side surface. The value of $J(O_2)$ is related to the permeation flux density as

$$J(O_2) = \frac{j \cdot d}{\ln(p_2/p_1)} \quad (19)$$

and is often suitable for the analysis of relative contributions of bulk diffusion and surface exchange to overall permeation process [29]. Being proportional to the permeation flux with subtracted $p(O_2)$ gradient term, it is also useful to evaluate the effects of change of concentration of mobile defects or their interactions on the oxygen

transport. As can be seen in Fig. 14, the specific oxygen permeability of iron-substituted ceramic membranes under (H$_2$–H$_2$O–N$_2$)/air gradients is several orders of magnitude higher compared to that under oxidizing conditions. This, in turn, implies several orders of magnitude higher oxygen-ionic conductivity under reducing conditions. The values of ionic conductivity at reduced $p(O_2)$ were estimated from the permeation data using relationship [50]:

$$\sigma_{amb}(p_1) = -\frac{16F^2d}{RT}\left[\frac{\partial j}{\partial \ln p_1}\right]_{p_2=const} \quad (20)$$

in combination with Eq. (18). The calculations showed that σ_O in $(La_{0.9}Sr_{0.1})_{0.98}Cr_{0.6}Fe_{0.3}Mg_{0.1}O_{3-\delta}$ reaches ~0.07 S cm^{-1} at 1223 K and $p(O_2) = 5 \times 10^{-18}$ and ~0.04 S cm^{-1} at 1173 K and $p(O_2) = 5 \times 10^{-19}$ atm. Thus, oxygen-ionic contribution to the total conductivity of $(La_{0.9}Sr_{0.1})_{0.98}Cr_{0.6}Fe_{0.3}Mg_{0.1}O_{3-\delta}$ corresponds to approximately 15–20% under these conditions. Comparison of oxygen permeability values for membranes with different iron content confirms also that iron substitution increases ionic transport under identical reducing conditions, in agreement with the oxygen nonstoichiometry data (Fig. 3B). One should note that the values of oxygen-ionic conductivity discussed in this subsection are only estimates calculated neglecting the contribution of surface exchange kinetics to the permeation process model. These values may be slightly underestimated compared to the true σ_O values due to non-negligible limiting effect of exchange rates.

3.8. Anodic performance of $(La_{0.9}Sr_{0.1})_{0.98}Cr_{0.6}Fe_{0.3}Mg_{0.1}O_{3-\delta}$

XRD pattern of $(La_{0.9}Sr_{0.1})_{0.98}Cr_{0.6}Fe_{0.3}Mg_{0.1}O_{3-\delta}$ powder calcined at 1473 K for 10 h and used for electrodes fabrication was found consistent with that of ceramic samples sintered at high temperatures and showed no phase impurities. The particle size of the powder and prepared electrodes was in the range 0.4–1.5 μm (Fig. 15A). Fig. 15B illustrates typical microstructure of $(La_{0.9}Sr_{0.1})_{0.98}Cr_{0.6}Fe_{0.3}Mg_{0.1}O_{3-\delta}$ porous layer on a solid electrolyte. The thickness of porous anodes was $\sim170-200$ μm, with CGO interlayer thickness corresponding to 4–6 μm.
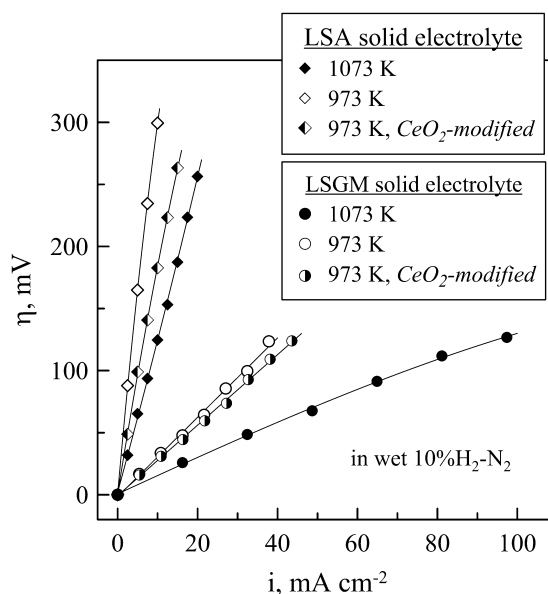

Fig. 16. Anodic polarization curves of $(La_{0.9}Sr_{0.1})_{0.98}Cr_{0.6}Fe_{0.3}Mg_{0.1}O_{3-\delta}$ porous electrode layers applied onto LSGM and LSA solid electrolytes with CGO interlayer and measured at 973–1073 K in humidified 10%H$_2$–N$_2$ atmosphere.

Table 7

Electrochemical performance of perovskite-type anodes in humidified 10%H$_2$–N$_2$ atmosphere.

Composition	T, K	R_η, Ω cm^2 (OCV conditions)	η, mV	Ref.
$(La_{0.9}Sr_{0.1})_{0.98}Ga_{0.8}Mg_{0.2}O_{3-\delta}$ solid electrolyte			$i = 30$ mA cm^{-2}	
$(La_{0.9}Sr_{0.1})_{0.98}Cr_{0.6}Fe_{0.3}Mg_{0.1}O_{3-\delta}$	1073	1.7	44	This work
	973	3.0	94	
$(La_{0.9}Sr_{0.1})_{0.98}Cr_{0.6}Fe_{0.3}Mg_{0.1}O_{3-\delta}$ (CeO$_2$-modified)	973	2.4	85	This work
$(La_{0.75}Sr_{0.25})_{0.95}Cr_{0.7}Fe_{0.3}O_{3-\delta}$	1073	1.2	35	[17]
$(La_{0.75}Sr_{0.25})_{0.95}Cr_{0.6}Fe_{0.4}O_{3-\delta}$	1073	1.6	44	[17]
$(La_{0.75}Sr_{0.25})_{0.95}Cr_{0.5}Mn_{0.5}O_{3-\delta}$	1073	2.8	73	[16]
$(La_{0.55}Sr_{0.45})_{0.95}Cr_{0.3}Mn_{0.5}Ti_{0.2}O_{3-\delta}$	1073	4.7	154	[23]
$La_{10}Si_5AlO_{26.5}$ solid electrolyte			$i = 20$ mA cm^{-2}	
$(La_{0.9}Sr_{0.1})_{0.98}Cr_{0.6}Fe_{0.3}Mg_{0.1}O_{3-\delta}$	1073	13	256	This work
	973	42	–	
$(La_{0.9}Sr_{0.1})_{0.98}Cr_{0.6}Fe_{0.3}Mg_{0.1}O_{3-\delta}$ (CeO$_2$-modified)	973	19	–	This work
$(La_{0.55}Sr_{0.45})_{0.95}Cr_{0.3}Mn_{0.5}Ti_{0.2}O_{3-\delta}$	1073	4.0	110	[23]
$(La_{0.25}Sr_{0.75})_{0.95}Mn_{0.5}Ti_{0.5}O_{3-\delta}$	1073	12	296	[23]

Fig. 16 demonstrates anodic polarization curves of porous $(La_{0.9}Sr_{0.1})_{0.98}Cr_{0.6}Fe_{0.3}Mg_{0.1}O_{3-\delta}$ anodes with CGO interlayers applied onto LSGM and LSA solid electrolytes. The electrochemical performance of these anodes in contact with LSGM electrolyte was found comparable to that of other Fe-substituted (La,Sr)CrO$_{3-\delta}$-based anodes and slightly better with respect to mixed chromite–manganite perovskites. Table 7 compares the characteristics (polarization resistance and overpotential values) of different perovskite-based anodes determined under identical electrochemical cell geometry and experimental conditions. One should note that all listed perovskite-like materials exhibit relatively low conductivity under anode operation conditions, 0.3–2.7 S cm^{-1} at 1123 K and $p(O_2) = 10^{-19}$–10^{-18} atm (Fig. 11A and Refs. [16,17,23]). Therefore, the relatively high resistivity of electrode layers under reducing conditions may indeed constitute a performance-limiting factor. This was confirmed, in particular, by the fact that the polarization resistance of $(La_{0.75}Sr_{0.25})_{0.95}Cr_{0.5}Mn_{0.5}O_{3-\delta}$ anode can be altered by more than an order of magnitude by changing current collector geometry (i.e. Pt wire vs. Pt gauze) [16]. On the other hand, there is no exact correlation between the values of polarization resistance (or overpotentials) and electrical conductivity of anode materials listed in Table 7. For instance, $(La_{0.9}Sr_{0.1})_{0.98}Cr_{0.6}Fe_{0.3}Mg_{0.1}O_{3-\delta}$ exhibits lowest conductivity but comparatively good electrochemical activity. This suggests non-negligible role of other factors such as interplay between ionic and electronic contributions as well as oxygen exchange kinetics. As for other materials [15,16,23], infiltration of ceria (loading ≤1 mg cm^{-2}), which is a mixed ionic-electronic conductor under reducing conditions and is also known for its electrocatalytic properties, into $(La_{0.9}Sr_{0.1})_{0.98}Cr_{0.6}Fe_{0.3}Mg_{0.1}O_{3-\delta}$ porous layer results in a moderate improvement of electrochemical behavior (Fig. 16 and Table 7).

Electrochemical measurements showed quite poor performance of $(La_{0.9}Sr_{0.1})_{0.98}Cr_{0.6}Fe_{0.3}Mg_{0.1}O_{3-\delta}$|CGO|LSA half-cells under anodic polarization. The polarization resistance under OCV conditions in reducing atmosphere corresponded to 13 Ω × cm^2 and rapidly increased with decreasing temperature (Table 7). Similar drop of electrochemical performance when applied onto lanthanum silicate-based solid electrolytes was reported earlier for a number of anode and cathode materials (e.g. Refs. [23,53] and references cited therein). Apart from the effect of solid electrolyte transport properties (e.g. lower conductivity of LSA compared to LSGM in high temperature range (Fig. 13B), much worse performance of electrode layers in contact with La$_{10-x}$Si$_6$O$_{26\pm\delta}$-based electrolytes was attributed to partial blocking of electrode reaction area by silica diffusing from electrolyte surface in the course of high-temperature electrode fabrication [23,53]. Apparently, similar blocking effects are responsible for the low electrochemical activity of $(La_{0.9}Sr_{0.1})_{0.98}Cr_{0.6}Fe_{0.3}Mg_{0.1}O_{3-\delta}$ in the present case, in spite of the presence of CGO interlayer. Surface modification with ceria results in ~2-fold decrease of polarization resistance and overpotentials (Fig. 16 and Table 7); still, the anode characteristics are far from the acceptable level.

3.9. Final remarks: comparison with other perovskite-type anode materials

In summary, Fe-substituted (La,Sr)(Cr,Mg)O$_{3-\delta}$ perovskites show favorably smaller chemical expansion compared to other chromites considered for anode applications (e.g. Refs. [16,17,23]). Oxygen-ionic conductivity in $(La_{0.9}Sr_{0.1})_{0.98}Cr_{0.9-x}Fe_xMg_{0.1}O_{3-\delta}$ ($x = 0.2$–0.3) under anode operation conditions is comparable to that of $(La_{0.75}Sr_{0.25})_{0.95}Cr_{1-x}Fe_xO_{3-\delta}$ ($x = 0.3$–0.4) [17] and is higher than in $(La_{0.75}Sr_{0.25})_{0.95}Cr_{0.5}Mn_{0.5}O_{3-\delta}$ [16]. Nevertheless, as for other chromite-based anodes, the electrochemical performance of iron-substituted LaCrO$_3$ electrodes is limited by insufficient level of ionic and electronic transport.

Due to phase stability requirements, the choice of other alternative perovskite-type materials for ceramic anodes is essentially limited to titanate-, molybdate- and vanadate-based systems. Similarly to LaCrO$_3$-based materials, Sr$_2$MoMgO$_6$ and donor-doped titanates show moderate TECs compatible with that of common solid electrolytes [3–5,54], while SrVO$_3$-based perovskites exhibit substantially higher thermal expansion [55]. High n-type electronic conductivity, >100 S cm^{-1}, is characteristic for donor-doped titanates (if reduced at high temperatures) and for SrVO$_3$ derivatives [3–5]. These materials exhibit, however, negligible (if any) ionic transport and are considered mainly as electronically-conducting components of composite anodes. Sr$_2$MoMgO$_6$ show relatively low electronic and ionic conductivity, 0.5–5 S cm^{-1} and 0.003 S cm^{-1} at 1073 K, respectively, but acceptable electrode performance [3–5,54]. The practical use of all these materials is currently restricted due to unresolved limitations, such as instability of SrVO$_3$ perovskite lattice under oxidizing conditions, questionable conductivity level in titanate materials under realistic electrode fabrication conditions, and decomposition of Sr$_2$MoMgO$_6$ under reducing conditions at ≥1173 K [3–5,55].

4. Conclusions

(i) XRD analysis confirmed the formation of single-phase $(La_{0.9}Sr_{0.1})_{0.98}Cr_{0.9-x}Fe_xMg_{0.1}O_{3-\delta}$ ($x = 0$–0.3) ceramics and electrodes. On heating in air, these oxides undergo a reversible transition from orthorhombic to rhombohedrally-distorted perovskite-type structure accompanied with minor dimensional changes. The structural transition is shifted to temperatures below ambient in reduced materials;

(ii) Thermogravimetric analysis, Mössbauer spectroscopy and electrical measurements in combination with XRD analysis confirmed the perovskite phase stability for composition with $x = 0.3$ down to the oxygen partial pressure as low as 10^{-19} atm at 1223 K;

(iii) Mössbauer spectroscopy results indicate that iron cations incorporated into chromium sublattice possess 3+ oxidation state under both oxidizing and reducing conditions;

(iv) Oxygen nonstoichiometry and defect chemistry of $(La_{0.9}Sr_{0.1})_{0.98}Cr_{0.6}Fe_{0.3}Mg_{0.1}O_{3-\delta}$ can be described by a non-ideal solution model in combination with site-exclusion effects;

(v) The total conductivity of $(La_{0.9}Sr_{0.1})_{0.98}Cr_{0.9-x}Fe_xMg_{0.1}O_{3-\delta}$ is predominantly electronic in the entire studied $p(O_2)$ range, with ionic contribution less than 0.001% at temperature below 1300 K under oxidizing conditions. The substitution with iron decreases electronic transport, but also leads to a higher oxygen deficiency and ionic conductivity under reducing conditions;

(vi) Thermal expansion coefficients of $(La_{0.9}Sr_{0.1})_{0.98}Cr_{0.9-x}Fe_x Mg_{0.1}O_{3-\delta}$ are nearly independent of $p(O_2)$ and iron content and are compatible with that of common solid electrolytes. Fe-substituted ceramics exhibits also a linear relationship between favorably small chemical strain and oxygen non-stoichiometry changes on reduction.

(vii) The electrochemical activity of $(La_{0.9}Sr_{0.1})_{0.98}Cr_{0.6}Fe_{0.3}Mg_{0.1}O_{3-\delta}$ porous anode layers applied onto LSGM electrolyte with CGO buffer interlayer in diluted hydrogen atmosphere is higher compared to $(La_{0.75}Sr_{0.25})_{0.95}Cr_{0.5}Mn_{0.5}O_{3-\delta}$ under similar conditions, and is limited by relatively low overall level of electronic and ionic transport. Poor electrochemical activity is observed in contact with LSA solid electrolyte.

Acknowledgments

References

[1] D. Sarantaridis, A. Atkinson, Fuel Cells 7 (2007) 246–258.
[2] Y. Matsuzaki, I. Yasuda, Solid State Ionics 132 (2000) 261–269.
[3] A. Orera, P.R. Slater, Chem. Mater. 22 (2010) 675–690.
[4] X.M. Ge, S.H. Chan, Q.L. Liu, Q. Sun, Adv. Energy Mater. 2 (2012) 1156–1181.
[5] E.V. Tsipis, V.V. Kharton, J. Solid State Electrochem. 15 (2011) 1007–1040.
[6] J.W. Fergus, Solid State Ionics 171 (2004) 1–15.
[7] J. Vulliet, B. Morel, J. Laurencin, G. Gauthier, L. Bianchi, S. Giraud, J.Y. Henry, F. Lefebvre-Joud, in: S.C. Singhal, M. Dokiya (Eds.), Solid Oxide Fuel Cells VIII, Electrochem. Soc. Series 2003–7, Electrochem. Soc. Inc., Pennington, 2003, pp. 803–811.
[8] R.T. Baker, I.S. Metcalfe, P.H. Middleton, B.C.H. Steele, Solid State Ionics 72 (1994) 328–333.
[9] A.L. Sauvet, J. Guindet, J. Fouletier, Ionics 5 (1999) 150–155.
[10] P. Vernoux, E. Djurado, M. Guillodo, J. Am. Ceram. Soc. 84 (2001) 2289–2295.
[11] S. Tao, J.T.S. Irvine, J. Electrochem. Soc. 151 (2004) A252–A259.
[12] X.J. Chen, Q.L. Liu, K.A. Khor, S.H. Chan, J. Power Sources 165 (2007) 34–40.
[13] D.M. Bastidas, S.W. Tao, J.T.S. Irvine, J. Mater. Chem. 16 (2006) 1603–1605.
[14] J. Wan, J.H. Zhu, J.B. Goodenough, Solid State Ionics 177 (2006) 1211–1217.
[15] S.P. Jiang, X.J. Chen, S.H. Chan, J.T. Kwok, J. Electrochem. Soc. 153 (2006) A850–A856.
[16] V.V. Kharton, E.V. Tsipis, I.P. Marozau, A.P. Viskup, J.R. Frade, J.T.S. Irvine, Solid State Ionics 178 (2007) 101–113.
[17] M.F. Lü, E.V. Tsipis, J.C. Waerenborgh, A.A. Yaremchenko, V.A. Kolotygin, S. Bredikhin, V.V. Kharton, J. Power Sources 206 (2012) 59–69.
[18] J. Peña-Martínez, D. Marrero-López, D. Pérez-Coll, J.C. Ruiz-Morales, P. Núñez, Electrochim. Acta 52 (2007) 2950–2958.
[19] S. Tao, J.T.S. Irvine, Chem. Mater. 16 (2004) 4116–4121.
[20] J.M. Haag, B.D. Madsen, S.A. Barnett, K.R. Poeppelmeier, Electrochem. Solid-State Lett. 11 (2008) B51–B53.
[21] M. Oishi, K. Yashiro, K. Sato, J. Mizusaki, T. Kawada, J. Solid State Chem. 181 (2008) 3177–3184.
[22] E.V. Tsipis, V.V. Kharton, J. Solid State Electrochem. 12 (2008) 1039–1060.
[23] V.A. Kolotygin, E.V. Tsipis, A.L. Shaula, E.N. Naumovich, J.R. Frade, S. Bredikhin, V.V. Kharton, J. Solid State Electrochem. 15 (2011) 313–327.
[24] J.C. Waerenborgh, D.P. Rojas, N.P. Vyshatko, A.L. Shaula, V.V. Kharton, I.P. Marozau, E.N. Naumovich, Mater. Lett. 57 (2003) 4388–4393.
[25] V.V. Kharton, M.V. Patrakeev, J.C. Waerenborgh, V.A. Sobyanin, S.A. Veniaminov, A.A. Yaremchenko, P. Gaczyński, V.D. Belyaev, G.L. Semin, J.R. Frade, Solid State Sci. 7 (2005) 1344–1352.
[26] J. Hesse, A. Rübartsch, J. Phys. E 7 (1974) 526–532.
[27] M.V. Patrakeev, I.A. Leonidov, V.L. Kozhevnikov, J. Solid State Electrochem. 15 (2011) 931–954.
[28] I.A. Leonidov, V.L. Kozhevnikov, E.B. Mitberg, M.V. Patrakeev, V.V. Kharton, F.M.B. Marques, J. Mater. Chem. 11 (2001) 1201–1208.
[29] A.V. Kovalevsky, A.A. Yaremchenko, V.A. Kolotygin, A.L. Shaula, V.V. Kharton, F.M.M. Snijkers, A. Buekenhoudt, J.R. Frade, E.N. Naumovich, J. Membr. Sci. 380 (2011) 68–80.
[30] R.D. Shannon, Acta Cryst. A32 (1976) 751–767.
[31] H. Hayashi, M. Watanabe, H. Inaba, Thermochim. Acta 359 (2000) 77–85.
[32] M. Mori, T. Yamamoto, H. Itoh, T. Watanabe, J. Mater. Sci. 32 (1997) 2423–2431.
[33] H. Hayashi, M. Watanabe, M. Ohuchida, H. Inaba, Y. Hiei, T. Yamamoto, M. Mori, Solid State Ionics 144 (2001) 301–313.
[34] P.D. Battle, T.C. Gibb, S. Nixon, J. Solid State Chem. 79 (1989) 75–85.
[35] P. Adler, U. Schwarz, K. Syassen, A.P. Milner, M.P. Pasternak, M. Hanfland, J. Solid State Chem. 155 (2000) 381–388.
[36] S. Onuma, K. Yashiro, S. Miyoshi, A. Kaimai, H. Matsumoto, Y. Nigara, T. Kawada, J. Mizusaki, K. Kawamura, N. Sakai, H. Yokokawa, Solid State Ionics 174 (2004) 287–293.
[37] J. Mizusaki, S. Yamauchi, K. Fueki, A. Ishikawa, Solid State Ionics 12 (1984) 119–124.
[38] H.U. Anderson, M.M. Nasrallah, B.K. Flandermeyer, A.K. Agarwal, J. Solid State Chem. 56 (1985) 325–334.
[39] F. Boroomand, E. Wessel, H. Bausinger, K. Hilpert, Solid State Ionics 129 (2000) 251–258.
[40] A. Zuev, L. Singheiser, K. Hilpert, Solid State Ionics 147 (2002) 1–11.
[41] M. Oishi, K. Yashiro, J.O. Hong, Y. Nigara, T. Kawada, J. Mizusaki, Solid State Ionics 178 (2007) 307–312.
[42] P.H. Larsen, P.V. Hendriksen, M. Mogensen, J. Therm. Anal. 49 (1997) 1263–1275.
[43] K. Hilpert, R.W. Steinbrech, F. Boroomand, E. Wessel, F. Meschke, A. Zuev, O. Teller, H. Nickel, L. Singheiser, J. Eur. Ceram. Soc. 23 (2003) 3009–3020.
[44] T.R. Armstrong, J.W. Stevenson, L.R. Pederson, P.E. Raney, J. Electrochem. Soc. 143 (1996) 2919–2925.
[45] R. Raffaelle, H.U. Anderson, D.M. Sparlin, P.E. Parris, Phys. Rev. B 43 (1991) 7991–7999.
[46] I. Yasuda, M. Hishinuma, Solid State Ionics 80 (1995) 141–150.
[47] E. Ahlgren, F.W. Poulsen, Solid State Ionics 70-71 (1994) 528–532.
[48] A. Atkinson, S. Barnett, R.J. Gorte, J.T.S. Irvine, A.J. McEvoy, M. Mogensen, S.C. Singhal, J. Vohs, Nat. Mater. 3 (2004) 17–27.
[49] T. Kawada, T. Horita, N. Sakai, H. Yokokawa, M. Dokiya, Solid State Ionics 79 (1995) 201–207.
[50] C.H. Chen, H. Kruidhof, H.J.M. Bouwmeester, A.J. Burggraaf, J. Appl. Electrochem. 27 (1997) 71–75.
[51] A.A. Yaremchenko, A.V. Kovalevsky, V.V. Kharton, Solid State Ionics 179 (2008) 2181–2191.
[52] H. Sasaki, M. Suzuki, A. Kajimura, in: B. Thorstensen (Ed.), Proceedings of Second European Solid Oxide Fuel Cell Forum, vol. 1, 1996, pp. 513–520.
[53] A.A. Yaremchenko, V.V. Kharton, D.O. Bannikov, D.V. Znosak, J.R. Frade, V.A. Cherepanov, Solid State Ionics 180 (2009) 878–885.
[54] Z. Xie, H. Zhao, Z. Du, T. Chen, N. Chen, X. Liu, S.J. Skinner, J. Phys. Chem. C 116 (2012) 9734–9743.
[55] A.A. Yaremchenko, B. Brinkmann, R. Janssen, J.R. Frade, Solid State Ionics 247–248 (2013) 86–93.